Enhancing Dihydrogen Interaction of a Zirconium Metal−Organic Framework by Metal Doping

Xiyuan Yao,[a] Sichi Li,[b,c,] Matthew J. Tang,[a] Hashim Al Khunaizi,[d] Long Qi,[e] Brandon C. Wood,[b,c] and Yangyang Liu[a,*]*

[a] Department of Chemistry and Biochemistry, California State University, Los Angeles, 5151 State University Drive, Los Angeles, California 90032, United States

[b] Materials Science Division, Lawrence Livermore National Laboratory, Livermore, California 94550, United States

[c] Laboratory for Energy Applications for the Future (LEAF), Lawrence Livermore National Laboratory, Livermore, California 94550, United States

[d] Department of Chemistry and Biochemistry, University of California, Los Angeles, Los Angeles California, 90095, United States

[e] U.S. DOE Ames National Laboratory, Iowa State University, Ames, Iowa 50011, United States

*Corresponding authors: yliu114@calstatela.edu (Y.L.); li77@llnl.gov (S.L.)

ABSTRACT

Advancing efficient hydrogen storage technologies is essential for enabling a sustainable energy future, especially in onboard applications. While hydrogen offers high gravimetric energy density and zero-emission combustion, its low volumetric energy density presents significant storage challenges. Metal-organic frameworks (MOFs), well known for their tunable porosity and high surface areas, have emerged as promising candidates for adsorption-based hydrogen storage. This study investigated a chemically robust zirconium-based MOF, MOF-808, as a representative platform for hydrogen storage enhancement through metal ion doping. Various divalent metal ions were introduced into MOF-808 via one-pot synthesis or post-synthetic modification (PSM) to evaluate their effects on metal doping efficiency, framework stability, and hydrogen adsorption performance. Our findings demonstrate that metal doping enhanced the hydrogen binding affinity of MOF-808 while preserving its structural integrity and excellent stability. A Mg-doped MOF, MOF-808@Mg 2:1, showed a 59% increase in hydrogen uptake, and a Cu-doped MOF, MOF-808-ZrCu, exhibited a 33% increase in isosteric heat of adsorption for H_2 compared to the pristine MOF-808 activated at the same temperature. This work highlights the potential of metal-functionalized stable MOFs for practical hydrogen storage applications.

KEYWORDS:

Hydrogen storage, metal-organic frameworks (MOFs), metal doping, open metal sites, one-pot synthesis, post-synthetic modification (PSM)

Introduction

Since the Industrial Revolution, the widespread reliance on fossil fuels has had a lasting negative impact on the environment, and it has become an urgent need to develop cleaner energy alternatives. Hydrogen (H_2) is considered a zero-emission energy carrier in fuel cell vehicles, as its combustion only releases water vapor instead of harmful pollutants such as carbon dioxide, nitrogen oxides, and particulate matter. Furthermore, hydrogen can be produced from a variety of renewable sources, such as water electrolysis powered by solar or wind energy, enabling a sustainable, circular energy cycle.[1-2] This makes hydrogen an ideal long-term replacement for petroleum in onboard applications.[3-4] Although challenges remain—particularly in terms of cost, storage, and infrastructure development—hydrogen holds significant potential to play a central role in the global transition to a low-carbon energy future.

Hydrogen boasts an impressive gravimetric energy density of 120 MJ/kg despite a notably low volumetric energy density of 0.01079 MJ/L.[5] Storing hydrogen under practical conditions presents a major challenge due to its low volumetric energy density. To achieve efficient energy storage and delivery, hydrogen must be either compressed to extremely high pressures (typically between 200 and 700 bar) or cooled to cryogenic temperatures (around −253 °C) for liquefaction.[6] Both approaches are currently used in a limited number of hydrogen-powered vehicles on the market; however, they come with significant drawbacks, including safety risk, high cost, and energy inefficiency. These limitations highlight the urgent need for safer and more practical storage solutions for H_2, especially in onboard applications. One promising strategy involves using porous adsorbent materials that can adsorb hydrogen at much milder conditions− lower pressures (under 100 bar) and ambient temperature.[7-8] A wide range of porous solids based on chemisorption and physisorption has been explored for this purpose. Chemisorption materials, such as metal-alloy

hydrides,[9] often exhibit high hydrogen storage capacities and good reversibility. However, their practical application is hindered by high thermodynamic stability and poor hydrogen absorption/desorption kinetics. These kinetic limitations are typically characterized as high hydrogenation/dehydrogenation temperatures, prolonged absorption/desorption durations, and high activation energies for dehydrogenation.[9-13] Common physisorption materials mainly include zeolites, carbon-based materials, covalent-organic frameworks (COFs), and metal-organic frameworks (MOFs).[14-16] MOFs, in particular, have attracted strong interest due to their crystalline nature and exceptional porosity. Composed of metal ions or clusters linked by organic molecules, these materials offer high surface areas, porosities, and tunable structures, making them especially effective for gas storage.[17-18]

H_2 is typically stored through physisorption with a hydrogen adsorption heat of 4.0 - 12.0 kJ/mol in most porous adsorbents, including MOFs.[19] Increasing the hydrogen adsorption heat is a viable approach to improving the hydrogen storage of adsorbents at ambient temperature.[20-21] To enhance hydrogen storage capacities and the hydrogen adsorption heat, MOFs featuring open metal sites, such as Mg or Cu-based MOFs, showed significant advantages due to their strong interactions with hydrogen molecules.[22-23] Charged metal centers could attract H_2 molecules and induce a dipole moment in the adsorbed H_2, serving as strong adsorption sites, especially at low pressure. It was reported that metal ions in MOFs exhibited an enhanced affinity for H_2 due to an energetic stabilization of the metal-H_2 interactions arising from the combination of *d* orbitals of the metal and the antibonding σ* orbital of the H_2.[21, 24]

However, the stability of most MOFs bearing open sites is often limited under ambient conditions, as the not fully coordinated metal centers are susceptible to water adsorption, hydrolysis, and subsequent structural degradation.[25-27] Conversely, MOFs with high valence

metals (e.g., Zr-MOF or Fe-MOF),[28] known for their exceptional chemical stability, typically lack open metal sites, resulting in relatively lower hydrogen uptake. To bridge this gap, recent studies have explored the incorporation of coordinatively unsaturated metal ions into highly stable MOFs to introduce open metal sites while maintaining their stability. For example, the development of NU-2100, a Cu(I)-based MOF synthesized using a Cu/Zn precursor mixture, has demonstrated air stability and high hydrogen storage capacity, with an isosteric heat of adsorption ($-\Delta H_{ads}^{0}$) of 32 kJ/mol under ambient conditions.[22] Earlier studies also incorporated various metal ions into Zr-based MOFs while preserving the framework stability; however, these studies primarily focused on exploring catalytic functions or tuning other physicochemical properties of the metal-doped MOFs.[29-30] For instance, Hou et al.[30] prepared metal-doped MOF-808-ZrM by adding transition metals during the synthesis of the MOF-808 and utilized the metal-doped MOF in toluene oxidation, which showed improved mobility and oxygen vacancy concentration in the MOF catalyst. Another study by Gil-San-Millan et al.[31] used post-synthetic modification (PSM) to incorporate Mg^{2+} into Zr-MOFs, including MOF-808 and NU-1000, to improve their catalytic activity for the detoxification of nerve agents. However, investigations specifically targeting gas adsorption enhancement through metal doping in Zr-MOFs remain scarce.

In this work, we systematically investigated how metal doping in a stable Zr-MOF affects its hydrogen adsorption properties. MOF-808 (**Figure 1**a), a well-known Zr-MOF constructed from Zr_6 metal-oxo clusters and 1,3,5-benzenetricarboxylic acid (BTC), was selected for metal doping due to its ease of synthesis and scale-up, and its remarkable stability in acidic, basic, and boiling aqueous environments.[32] Various divalent metal cations, including Mn^{2+}, Cu^{2+}, $Ca^{2+,}$ and Mg^{2+}, were introduced into MOF-808 via two different metal-doping strategies − one-pot synthesis (**Figure 1**b) and post-synthetic modification (PSM) (**Figure 1**c). We then studied the effect of

metal ions on the degree of metal doping, MOF stability, and hydrogen adsorption properties. Our findings demonstrate that metal doping enhanced the hydrogen binding affinity of MOF-808 while preserving its structural integrity and excellent stability. Remarkably, a Mg-doped MOF, MOF-808@Mg 2:1, showed a 59% increase in hydrogen uptake, and a Cu-doped MOF, MOF-808-ZrCu, exhibited a 33% increase in isosteric heat of adsorption ($-\Delta H_{ads}^{0}$) for H_2 compared to the pristine MOF-808 activated at the same temperature. Density functional theory (DFT) calculations revealed that these enhancements were attributed to the easily generated divalent open metal sites introduced into the Zr-MOF via metal doping. To our knowledge, this work is the first to demonstrate the feasibility of introducing open metal sites into Zr-MOFs for enhanced hydrogen adsorption.

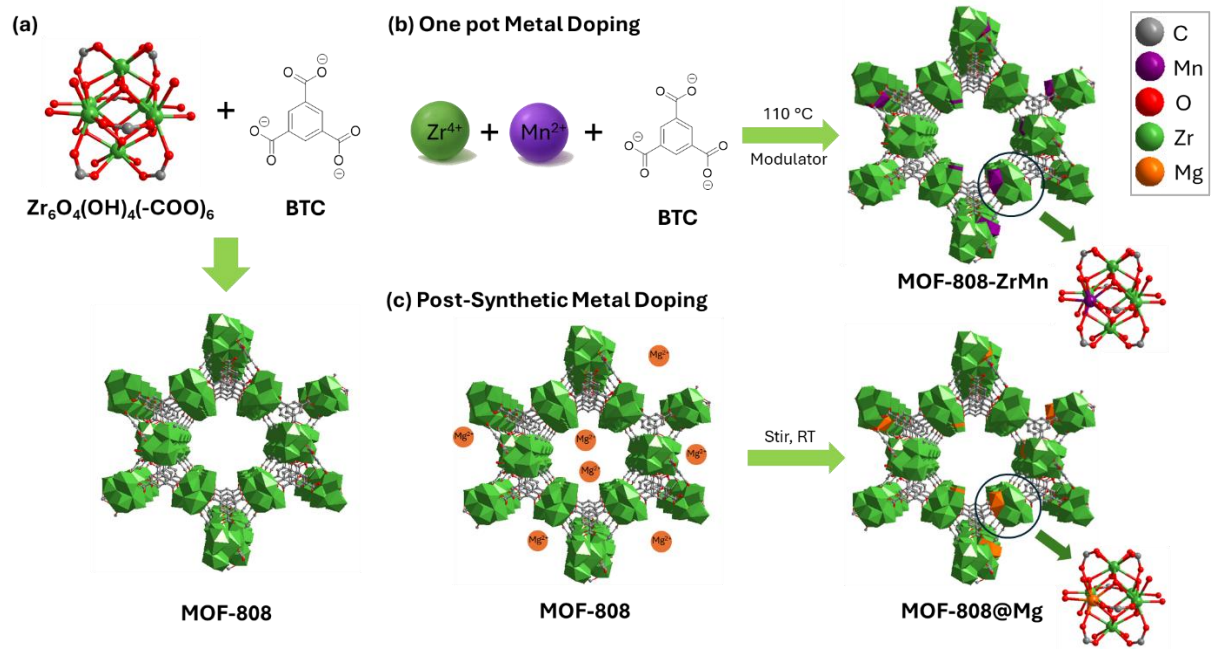

Figure 1 (a) Structures of $Zr_6O_4(OH)_4(-COO)_6$ nodes, the 1,3,5-benzenetricarboxylate (BTC) linker, and MOF-808. Schematic representation of (b) one-pot and (c) post-synthetic metal doping of MOF-808. H atoms are omitted for clarity.

Experimental section

Chemicals and materials

Benzoic acid (99.5%), calcium nitrate hexahydrate ($Ca(NO_3)_2 \cdot 6H_2O$, 98%), methanol (MeOH, 99.8%), acetone (99.5%), and *N, N*'-dimethylformamide (DMF, 99.9%) were purchased from Fisher Scientific. Manganese nitrate tetrahydrate ($Mn(NO_3)_2 \cdot 4H_2O$, 98%) and copper nitrate hemi(pentahydrate) ($Cu(NO_3)_2 \cdot 2.5H_2O$, 98%) were purchased from Alfa Aesar. Zirconyl chloride octahydrate ($ZrOCl_2 \cdot 8H_2O$, 98%) was purchased from Acros Organics. 1,3,5-benzenetricarboxylic acid (H_3BTC, 98%) was purchased from TCI America. Magnesium methoxide solution ($Mg(OMe)_2$, 6-10 wt% in methanol) was purchased from Sigma-Aldrich. All chemicals were used without further purification.

Synthesis of Pristine MOF-808

The pristine MOF-808 was synthesized following a published literature procedure reported by Dai et al..[33] 1,3,5-benzenetricarboxylic acid (149 mg, 0.7 mmol) was added to DMF (12.8 mL) in a 40 mL vial while stirring at 600 rpm. $ZrOCl_2 \cdot 8H_2O$ (216 mg, 0.67 mmol) and formic acid (13.3 mL) were subsequently added, and the reaction mixture was stirred for 20 min at room temperature. The vial was then heated at 110 °C for 48 h. A white solid was collected and washed in DMF and acetone three times each. MOF samples were dried in a vacuum oven at 50 °C overnight before activation on the degassing port of an ASAP2020 Plus.

One-pot synthesis of MOF-808-ZrM

MOF-808-ZrM was synthesized following published literature procedures.[30, 33] As an example, for the preparation of MOF-808-ZrMn, 1,3,5-benzenetricarboxylic acid (149 mg, 0.7 mmol) was added to DMF (12.8 mL) in a 40 mL vial while stirring at 600 rpm. $ZrOCl_2 \cdot 8H_2O$ (216 mg, 0.67 mmol), $Mn(NO_3)_2 \cdot 6H_2O$ (63 mg, 0.22 mmol), and formic acid (13.3 mL) were subsequently

added, and the reaction mixture was stirred for 20 min at room temperature. The vial was then heated at 110 °C for 48 h. A white solid was collected and washed in DMF and acetone three times each. MOF samples were dried in a vacuum oven at 50 °C overnight before activation on the degassing port of an ASAP2020 Plus. MOF-808-ZrCu and MOF-808-ZrCa were synthesized using similar procedure by replacing $Mn(NO_3)_2{\cdot}4H_2O$ with $Cu(NO_3)_2{\cdot}2.5H_2O$ and $Ca(NO_3)_2{\cdot}6H_2O$, respectively.

Post-synthetic synthesis of Mg-doped MOF-808

$Mg(OMe)_2$ functionalized Zr-MOF materials, designated as MOF-808@Mg, were prepared following published literature procedures.[31] By controlling the Zr_6 (cluster): Mg molar ratio (i.e., 1:1, 2:1, and 3:1), MOF-808@Mg with varied amounts of Mg was prepared. For example, in the case of MOF-808@Mg 1:1, 50 mg of dry MOF-808 was added to a methanolic solution of 49 μL of commercial 8 wt% $Mg(OMe)_2$/MeOH solution diluted with 2.5 mL of anhydrous and degassed MeOH in the glovebox, and the suspension was stirred for 15 min at room temperature. The resulting product was washed three times with anhydrous MeOH (15 mL) and dried in a vacuum oven at 50 ºC overnight, yielding 40 mg of MOF-808@Mg 1:1.

Materials characterizations

Powder X-ray diffraction (PXRD) patterns were collected on a D2 Phaser (Bruker Corporation) equipped with a Cu-sealed tube (λ = 1.54178 Å) at 30 kV and 10 mA, a step size of $2\theta = 0.02°$ (5 s per step) over a 2θ range of 2 to 20°. Inductively coupled plasma-optical emission spectroscopy (ICP-OES) was collected on an Agilent 5110 ICP-OES with SPS 4 Autosampler. Thermogravimetric analysis (TGA) was conducted using a TA Instruments Discovery TGA 55. For each thermal curve, 3-5 mg of sample were placed on a 100 μL platinum pan and allowed to reach 700 °C at a ramp rate of 10 °C/min under nitrogen with a flow rate of 40 ml/min. Scanning

electron microscopy (SEM) images were acquired on an FEI Quanta-FEG 250 field-emission SEM microscope. N_2/H_2 sorption data and the Brunauer-Emmett-Teller (BET) surface areas of all MOF samples were measured on a Micromeritics ASAP2020 Plus. FTIR spectra were measured on a Nicolet 6700 spectroscopy using an MCT detector. The spectra were collected in the range from 4000 to 600 cm^{-1} with a resolution of 1 cm^{-1} and 4 scans. Transmission electron microscope (TEM) images were recorded using the FEI Titan Themis with an aberration-corrected, monochromated, transmission electron microscope operated at 200 kV. The X-ray photoelectron spectroscopy (XPS) measurements were performed using a Kratos Amicus/ESCA 3400 instrument.

The heat of adsorption calculations

The H_2 adsorption isotherms measured at two different temperatures (77 K and 87 K) were fitted with virial fitting simultaneously (**equation (1)**),[34] and various numbers of *a* and *b* parameters were tested in the fitting procedure to obtain the optimal result. In our study, models incorporating 2–4 *a* parameters and 1–2 *b* parameters demonstrated an excellent fit to the isotherm data, with coefficients of determination (R^2) consistently exceeding 0.999. From the virial fit, $\Delta H_{ads}(n)$ was then calculated by multiplying the ideal gas constant *R* with the sum of the a_i coefficients multiplied by the uptake n to the power of *i* (**equation (2)**). The heat of adsorption at zero coverage (ΔH_{ads}^0) was well approximated by the multiplication of the ideal gas constant *R* (8.314 J mol^{-1} K^{-1}) and the first virial coefficient a_0 (**equation (3)**).

$$\ln p = \ln n + \frac{1}{T}\sum_{i=0}^{m} a_i n^i + \frac{1}{T}\sum_{i=0}^{m} b_i n^i \quad (1)$$

$$\Delta H_{ads}(n) = R \times \sum_{i=0}^{m} a_i n^i \quad (2)$$

$$\Delta H_{ads}^0(n) = R \times a_0 \quad (3)$$

Density functional theory calculations

Plane-wave, periodic supercell density functional theory (DFT) calculations were carried out using the Vienna *ab initio* Simulation Package (VASP), version 5.4.4,[35] employing the projector augmented wave (PAW) method for treating core-valence interactions.[36-37] The exchange-correlation energy was described using the nonlocal rev-vdW-DF2[38] functional, which has been reported to yield accurate binding energies in MOFs.[39] The initial periodic structure of MOF-808 was adopted from the computational study by Yang et al..[40] The Mg-doped MOF-808 model was constructed by substituting one Zr atom with an Mg atom, followed by converting the –OH ligand bound to Mg to an H_2O ligand and one bridging –O ligand to –OH, to account for the divalent nature of Mg^{2+}. Full lattice and ionic relaxations were conducted with a plane-wave energy cutoff of 520 eV, a self-consistent field (SCF) energy convergence criterion of 10^{-6} eV for total energy, and a force convergence threshold of 0.01 eV/Å. H_2 binding energies ($\Delta E_{H2\ binding}$) and H_2O desorption energies ($\Delta E_{H2O\ desorption}$) were computed following (equation (4) and (5)):

$$\Delta E_{H2\ binding} = E_{MOF\text{-}808+H2} - E_{MOF\text{-}808} - E_{H2} \quad (4)$$

$$\Delta E_{H2O\ desorption} = E_{MOF\text{-}808} - E_{MOF\text{-}808\text{–}2H2O} - 2E_{H2O} \quad (5)$$

where $E_{MOF\text{-}808+H2}$, $E_{MOF\text{-}808}$, E_{H2}, $E_{MOF\text{-}808\text{–}2H2O}$, E_{H2O} are DFT-computed 0-K energies of MOF 808 with an H_2 adsorbate, clean MOF-808, gas-phase H_2, MOF-808 with 2 H_2O desorbed from a Zr/Mg site, gas phase H_2O, respectively.

Results and discussion

Pristine MOF-808

MOF-808 (**Figure 1**a) is a zirconium-based MOF constructed from $Zr_6O_4(OH)_4$ secondary building units (SBUs) coordinated with 1,3,5-benzenetricarboxylate (BTC) linkers. In a defect-free MOF-808 structure, each Zr_6 node in MOF-808 is connected to six carboxylate groups from BTC ligands, resulting in a robust and highly porous framework with 6-connected Zr_6 nodes. The structure features a large tetrahedral cage, resulting in high surface area and pore volume. The pristine MOF-808 was synthesized following a published literature procedure reported by Dai et al..[33] The structure, phase purity, and crystallinity of the pristine MOF-808 were confirmed by powder X-ray diffraction (PXRD) (**Figure S1**). TEM and SEM images revealed nanosized particles of the pristine MOF-808 with an average particle size of 50-100 nm (**Figures 2a and S2**).

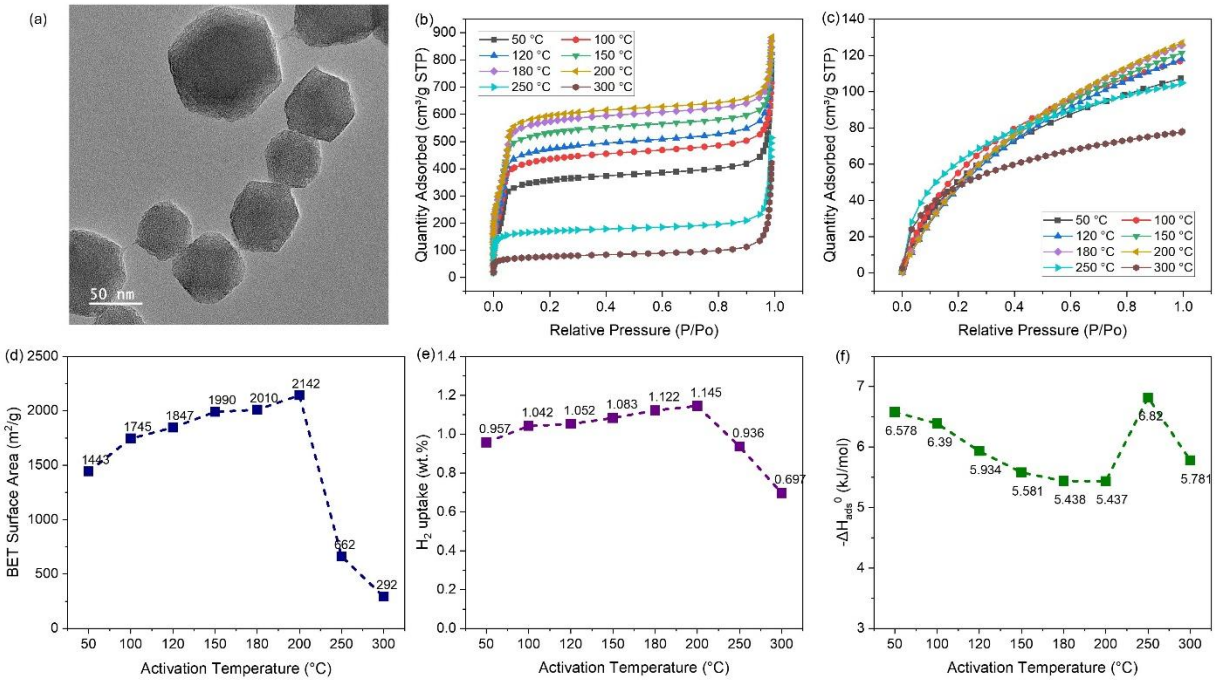

Figures 2 (a) TEM image, (b) N_2 adsorption isotherms at 77 K, and (c) H_2 adsorption isotherms at 77 K up to 1 bar for pristine MOF-808; Summaries of BET surface areas (d), wt.% H_2 adsorbed

at 1 bar/77 K (e), and the heat of adsorption ($-\Delta H_{ads}^{0}$) for H_2 (f) of pristine MOF-808 activated at various temperatures.

Since different activation temperatures can affect the extent of free and coordinated solvent evaporation, determining the optimal activation temperature is essential for maximizing the H_2 adsorption capacity of a MOF. To study the effect of activation temperature on MOF-808's surface area, H_2 uptake, and heat of adsorption, MOF-808 was heated under vacuum at varied temperatures ranging from 50 °C to 300 °C. As shown in **Figures 2**b, the N_2 adsorption of pristine MOF-808 exhibited a reversible Type I isotherm, indicating its microporous nature. When the activation temperature increased from 50 ºC to 200 ºC, the BET surface area and H_2 uptake of the MOF-808 increased accordingly due to the removal of free and coordinated solvents in the MOF (**Figure 2**de and **Table S1**). Interestingly, the heat of adsorption values ($-\Delta H_{ads}^{0}$) for H_2 decreased with increasing activation temperature from 50-200 °C, suggesting that the removal of free and coordinated solvent molecules weakened the MOF's binding affinity to H_2 (**Figures 2**f and **Table S1**). This observation may be attributed to the smaller pores that the coordinated solvents created in the MOF, contributing to stronger van der Waals interactions with H_2. Furthermore, when the activation temperature continued to increase to 250-300 ºC, the N_2 and H_2 adsorption capacities started to decline quickly (**Figures 2**bcde), indicating that the MOF structure started to lose its porosity at activation temperatures above 200 °C. This decrease in porosity was attributed to partial to substantial structural collapse of MOF-808 at elevated temperature, which was validated by PXRD patterns of the activated MOFs (**Figures S3**). MOF-808 activated at 200 °C showed similar PXRD pattern and FT-IR spectrum as the as-synthesized MOF-808 (**Figures S3 and S4**), indicating preservation of crystallinity and structure after removing coordinated water/solvent ligands on Zr_6 clusters at 200 °C, which explains the highest N_2 and H_2 adsorption for samples

activated at this temperature (**Figure 2**). In contrast, MOF-808 activated at 250 and 300 °C lost most or all of their crystallinity, evidenced by the significant decrease or disappearance of diffraction peaks in the PXRD patterns for these samples (**Figure S3**). FT-IR spectrum of MOF-808 activated at 250 °C exhibited an intensity decrease for the peak at around 649 cm^{-1}, corresponding to Zr-O-Zr bond in the Zr_6 node (**Figure S4**). Due to the partial or substantial structural collapse in these samples after losing possibly bridging ligands at 250-300 °C, lower N_2 and H_2 adsorption capacities were observed (**Figure 2**).

It is worth noting that despite the decrease in porosity and H_2 uptake, MOF-808 activated at 250 ºC exhibited the highest $-\Delta H_{ads}^0$ value for H_2 (6.82 kJ/mol; **Figure 2**f) compared to samples activated at other temperatures. This observation can be attributed to the open Zr sites generated by removing a substantial amount of coordinated water/solvent ligands on the Zr_6 clusters at 250 ºC. These results showed that structure collapse affected the porosity of MOF-808 but did not compromise its open metal sites. Even though MOF-808 activated at 250 ºC showed a lower total H_2 adsorption capacity due to partial structural collapse, a higher amount of open metal sites generated at this temperature is able to form stronger interactions with H_2, evidenced by the higher heat of adsorption observed at 250 ºC. The relatively higher H_2 adsorption under low partial pressure (0-0.3 bar) for MOF-808 activated at 250 ºC is another evidence of a stronger H_2 interaction induced by more open Zr sites (**Figure S5**). When the activation temperature further increased to 300 ºC, MOF-808 lost most of its porosity and showed the lowest H_2 uptake due to a higher degree of structural collapse (**Figures 2**bd). Nevertheless, a decent $-\Delta H_{ads}^0$ of 5.78 kJ/mol was still observed for this sample due to some remaining open Zr sites (**Figures 2**f).

Essentially, the above results showed that higher activation temperature allows the generation of more open Zr sites in pristine MOF-808, increasing its affinity to H_2 molecules. However, higher

activation temperature can also cause structural collapse and compromise the surface area and H_2 adsorption capacity of MOF-808 (250-300 °C). To resolve this dilemma, we sought to introduce secondary open metal sites into Zr-MOF structures, allowing the enrichment of open metal sites in stable MOFs without compromising MOF structures. This approach is expected to improve Zr-MOF's interaction with hydrogen through the secondary open metal sites while retaining the MOF's high porosity, high hydrogen adsorption capacity, and exceptional hydrolytic/chemical stability. To test our hypothesis, various divalent metal ions, including Mn^{2+}, Cu^{2+}, and Ca^{2+}, were introduced to MOF-808 with one-pot synthesis, and Mg^{2+} was introduced to MOF-808 using post-synthetic doping. We chose divalent metal sites because: 1) they were reported to have a favorable interaction with H_2 in porous materials,[22-23] 2) their relatively weaker coordination with oxygen-containing terminal groups compared to Zr^{4+} (due to their lower hardness according to Hard and Soft Acid and Base (HSAB) Principle) could facilitate solvent dissociation and open metal site generation at lower activation temperatures.

One-pot metal-doped MOF-808-ZrM

In the one-pot synthesis of metal-doped MOF-808, we used a 2:1 molar ratio of the secondary metal ions to the Zr_6 cluster, which was reported to be the optimal ratio for MOF formation.[30] PXRD of the MOF-808-ZrM samples showed similar patterns as that of the pristine MOF-808, confirming that their structure and crystallinity were maintained after metal doping (**Figures 3a**). SEM images of the synthesized MOF-808-ZrM showed nanosized particles (**Figure S6**), and their size is consistent with pristine MOF-808. ICP-OES was used to confirm the successful incorporation of the secondary metal ions in MOF-808 for all samples (**Table S2**). Thermogravimetric analysis (TGA) profiles of the metal-doped MOF-808 showed a higher weight% loss than the pristine MOF-808 up to 400 °C (**Figure S7**), suggesting terminal ligands

on the metal-doped MOFs dissociated at lower temperatures than the pristine MOF, confirming our hypothesized labile nature of the doped divalent metals. All MOFs underwent complete structural decomposition around 450-500 °C (ligand dissociation and carbonization), and MOF-808-ZrCu exhibited slightly higher thermal stability than the other three.

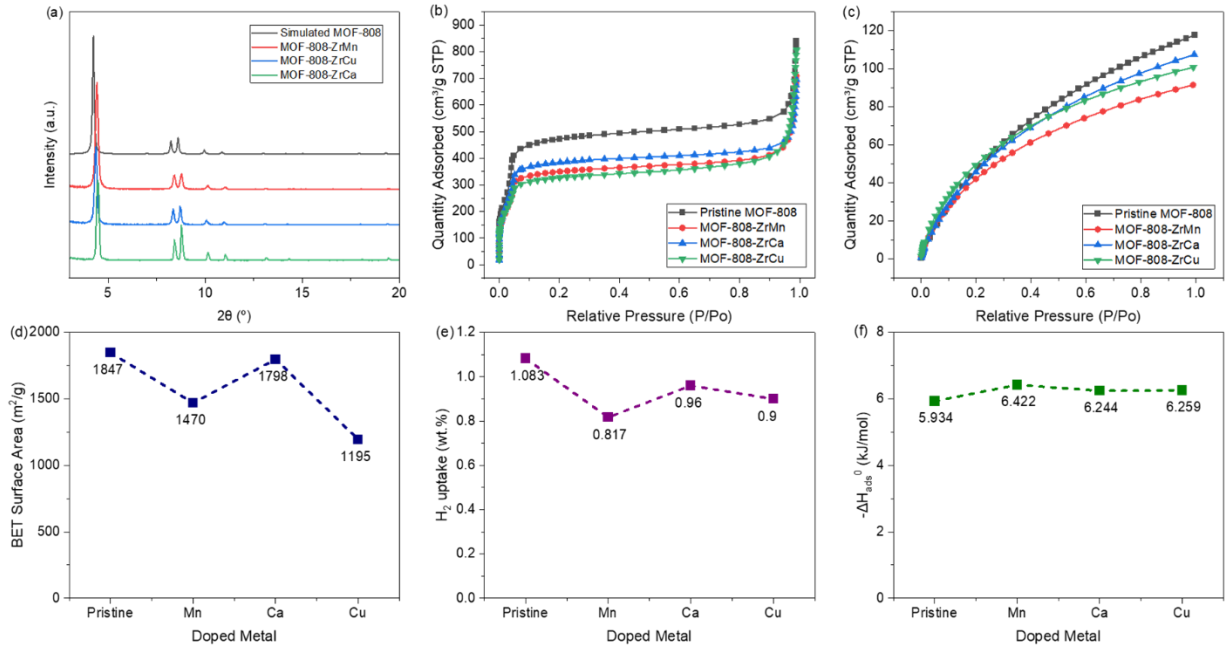

Figures 3 (a) PXRD patterns of MOF-808-ZrM compared to the simulated pattern of pristine MOF-808; (b) N_2 adsorption isotherms at 77 K, and (c) H_2 adsorption isotherms at 77 K up to 1 bar for MOF-808-ZrCu compared to pristine MOF-808; Summaries of BET surface areas (d), wt.% H_2 adsorbed at 1 bar/77K (e), and the heat of adsorption ($-\Delta H_{ads}^0$) (f) of metal-doped MOF-808-ZrM (M = Mn, Ca, and Cu) obtained through one-pot synthesis compared to pristine MOF-808.

After confirming the successful synthesis of MOF-808-ZrM (M = Cu^{2+}, Ca^{2+}, and Mn^{2+}), we activated all samples at 120 °C for 10 h and studied their gas sorption properties. The N_2 sorption isotherms at 77 K and corresponding BET surface areas of MOF-808-ZrM are summarized in **Figures 3** and **Table S3**. The metal-doped MOFs generally showed lower surface areas than the pristine MOF-808 activated under the same conditions (**Figure 3**bd). The H_2 isotherms at 77 K

(**Figures 3**c) and 87 K of MOF-808-ZrM were also measured, and the MOFs' heat of adsorption for H_2 was calculated (**Figures 3**f and **Table S3**). Compared to the pristine MOF-808, the metal-doped MOF-808-ZrM activated at the same temperature showed lower H_2 uptake, which aligns with their lower surface areas. However, the metal-doped MOF-808-ZrM all exhibited a 12-15% enhancement in their heat of adsorption ($-\Delta H_{ads}^0$) for H_2, validating our hypothesis that open metal sites incorporated into Zr-MOFs can enhance their interactions with H_2. Moreover, MOF-808-ZrM showed superior stability to traditional MOFs bearing open metal sites. The PXRD patterns of the samples stored under ambient conditions after a month and those soaked in aqueous solutions for a week matched well with the simulated pattern of MOF-808 (**Figures S8** and **S9**). Among all three doped MOFs, MOF-808-ZrCu showed the highest adsorption affinity for H_2 under low partial pressure (0-0.3 P/P_o) (**Figure S10**) and considerable H_2 uptake at 77 K and 1 bar. Therefore, we selected this MOF for further studies on the effect of various activation temperatures later.

Post-synthetic Mg-doped MOF-808

In addition to using one-pot synthesis, Mg^{2+} was incorporated into MOF-808 post-synthetically by reacting the pristine MOF-808 with $Mg(OMe)_2$ solutions of varied concentrations. Three Mg-doped MOF-808 samples were prepared by varying the Zr_6 cluster to Mg^{2+} ratio (1:1, 2:1, and 3:1) in the MOF/$Mg(OMe)_2$ suspension. The resulting Mg-doped MOFs are named as MOF-808@Mg1:1, MOF-808@Mg2:1, and MOF-808@Mg3:1, respectively. PXRD patterns of all three MOF-808@Mg samples are in good agreement with the simulated pattern of pristine MOF-808, indicating that the MOF-808 structure was retained after post-synthetic metal doping (**Figure 4a**). SEM images of the synthesized MOF-808@Mg showed nanosized particles (**Figure S11**), and their sizes are consistent with pristine MOF-808. The amount of Mg^{2+} introduced into MOF-808 was quantified using ICP-OES (**Table S4**), showing that MOF-808@Mg prepared using the

solution containing Zr_6:Mg = 2:1 incorporated the highest amount of Mg^{2+} (molar ratio of Mg/Zr_6 = 0.361). In addition, X-ray photoelectron spectroscopy (XPS) was used to confirm the incorporation of Mg^{2+} onto MOF-808 (**Figure S12**). As shown in Figure S11c, the XPS of Zr displayed two peaks at approximately 183 and 185 eV, corresponding to the $3d_{5/2}$ and $3d_{3/2}$ orbitals of Zr atoms in the Zr_6 cluster, respectively. For Mg-doped MOF-808, the peak at 183 eV showed a slightly downward shift compared with the pristine MOF-808, indicating the successful incorporation of Mg^{2+} into MOF-808. Furthermore, the as-synthesized pristine MOF-808 and metal-doped MOF-808 showed similar XPS results as those were activated at 250 °C, suggesting that Zr centers remain as Zr^{4+} after Mg^{2+} doping and after activation at 250 °C. Lastly, TGA results (**Figure S13**) showed a higher weight% loss for all three MOF-808@Mg samples than the pristine MOF-808, suggesting easier removal of coordinated water/solvent in the metal-doped MOFs. All MOFs underwent complete degradation at around 450-500 °C.

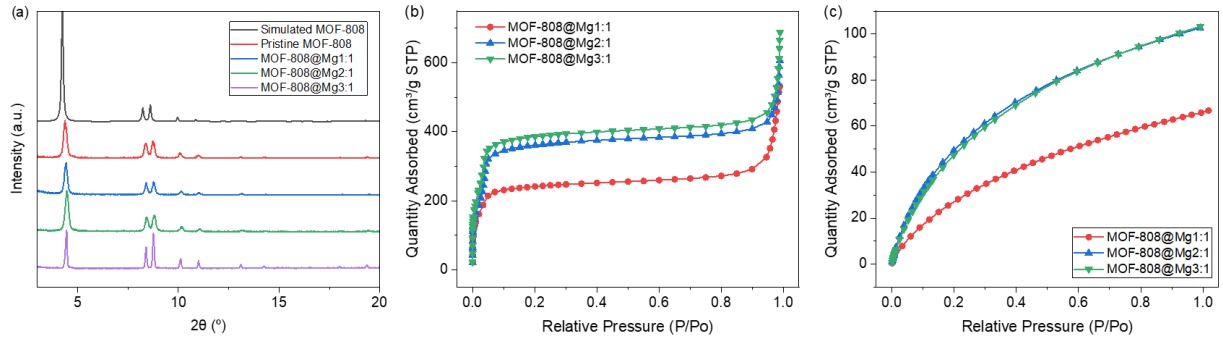

Figure 4 (a) PXRD patterns of post-synthetic metal-doped MOF-808@Mg compared to simulated and experimental patterns of pristine MOF-808; (b) N_2 adsorption isotherms at 77 K and (c) H_2 adsorption isotherms at 77 K up to 1 bar of post-synthetic Mg-doped MOF-808@Mg samples that were prepared using solutions with varied Zr_6:Mg ratios (1:1, 2:1, 3:1).

After activation at 50 °C for 5 hours, the N_2 sorption isotherms of MOF-808@Mg1:1, MOF-808@Mg2:1, and MOF-808@Mg3:1 were measured at 77 K (**Figure 4**b) to confirm the MOF

porosity. With H_2 adsorption measured at 77 K (**Figure 4**c) and 87 K, the heat of adsorption was calculated for three metalated MOFs. Their BET surface area, H_2 uptake, and heat of adsorption are summarized in **Table S5**. Among the three samples with different Mg loading, MOF-808@Mg2:1, with the highest Mg^{2+} loading, exhibited the highest heat of H_2 adsorption and highest H_2 adsorption at low partial pressure (0-0.3 P/P_o) (**Figure S14**). Its H_2 uptake at 1 bar and 77 K is comparable to MOF-808@Mg3:1. Therefore, we selected MOF-808@Mg2:1 for further studies involving different activation temperatures.

The effect of activation temperatures

To investigate whether the doped metal ions in MOF-808 play a role in H_2 adsorption and interaction, we studied two of our most promising metal-doped samples, Cu-doped MOF-808-ZrCu and Mg-doped MOF-808@Mg2:1, at various activation temperatures. TEM images showed preservation of MOF-808 particle shapes after Cu-doping (**Figure 5a**). Like the pristine MOF-808, increasing surface area and H_2 uptake for MOF-808-ZrCu were also observed when increasing activation temperature from 120 to 200 °C (**Figure 5**bcde). Notably, the metal-doped MOF-808-ZrCu also exhibited an increasing heat of H_2 adsorption ($-\Delta H_{ads}^0$) when activation temperatures increased from 50 to 200 °C (**Figure 5f** and **Table S6**), which is different from pristine MOF-808. These results suggest successful incorporation and generation of open Cu sites in MOF-808-ZrCu at moderate activation temperatures below 200 °C. As the activation temperature increased from 50-200 °C, an increasing amount of open Cu sites in MOF-808-ZrCu were generated, leading to higher H_2 uptake and heat of adsorption ($-\Delta H_{ads}^0$). On the other hand, most open Zr sites in pristine MOF-808 were not generated until 250 °C; at this point, the pristine MOF-808 had lost its structural integrity and thus showed lower total H_2 uptake, as we previously discussed.

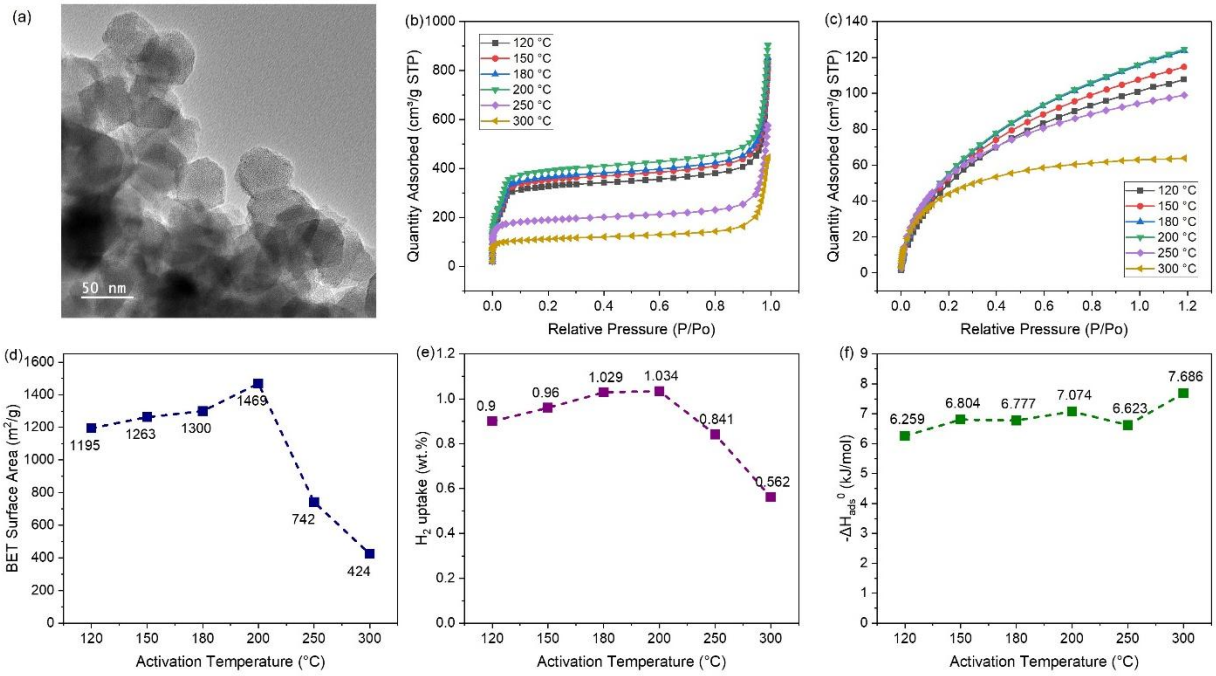

Figure 5 (a) TEM image, (b) N_2 adsorption isotherms at 77 K, and H_2 adsorption isotherms at 77 K up to 1 bar for Cu-doped MOF-808-ZrCu; Summaries of BET surface areas (d), wt.% H_2 adsorbed at 1 bar/77K (e) and the heat of adsorption ($-\Delta H_{ads}^0$) (f) of Cu-doped MOF-808-ZrCu activated under different temperatures.

When the activation temperature was further elevated to 250-300 °C, the porosity and H_2 uptake of MOF-808-ZrCu started to decline, consistent with what was observed for pristine MOF-808 (**Figure 5**). Loss of diffraction peaks in the PXRD patterns of MOF-808-ZrCu activated at 250 and 300 °C suggested structural collapse at elevated temperatures (**Figure S15**). However, decent heat of adsorption ($-\Delta H_{ads}^0$ = 6.623 kJ/mol) and high H_2 adsorption under low partial pressure (0-0.15 P/P_o) were observed for MOF-808-ZrCu activated at 250 °C (**Figures 5**f **and S16**), indicating the presence of open metal sites at 250 °C despite the decline in surface area and porosity. Interestingly, when activated at 300 °C, MOF-808-ZrCu showed the highest heat of adsorption ($-\Delta H_{ads}^0$) of 7.686 kJ/mol for H_2 compared to the same sample activated at lower temperatures.

Remarkably, compared to the pristine MOF-808 activated at 300 °C, MOF-808-ZrCu achieved a 33% increase in the heat of adsorption ($-\Delta H_{ads}^0$) for H_2, owing to the additional open sites introduced by metal doping.

We then investigated the gas sorption properties of MOF-808@Mg2:1 activated at different temperatures. TEM showed that the crystal shape of MOF-808 was preserved after post-synthetic Mg-doping (**Figure 6**a). As the activation temperature increased from 50 to 200 °C, the BET surface area and H_2 uptake of MOF-808@Mg2:1 increased, consistent with trends observed for pristine MOF-808 and one-pot doped MOF-808-ZrCu (**Figure 6**bcde). Above 250 °C, N_2 adsorption and BET surface area MOF-808@Mg2:1 began to decline due to partial structural collapse, as evidenced by its PXRD patterns (**Figure S17**). Interestingly, as the activation temperature increased from 200 to 250 °C, the H_2 uptake of MOF-808@Mg2:1 continued to improve, unlike the decline observed in pristine MOF-808. Compared to the pristine MOF-808 activated at 250 °C, H_2 uptake and heat of adsorption ($-\Delta H_{ads}^0$) of MOF-808@Mg2:1 increased by 38% and 4%, respectively. These enhancements in both H_2 uptake and heat of adsorption ($-\Delta H_{ads}^0$) in MOF-808@Mg2:1 can be attributed to the simultaneous generation of open Mg metal sites and Zr sites at 250 °C, which remain highly effective for H_2 adsorption despite the partial framework collapse. When the activation temperature was further elevated to 300 °C, the further compromised framework structure led to lower H_2 uptake as expected (**Figure 6**e). The structural collapse was confirmed by PXRD (**Figure S17**), but MOF-808@Mg2:1 still maintained a decent heat of adsorption ($-\Delta H_{ads}^0$) of 6.898 kJ/mol for H_2 (**Figure 6**f). The stronger MOF-H_2 interaction enabled by the additional open metal sites in the MOF-808@Mg2:1 activated at 250 and 300 °C was also observed in the H_2 adsorption isotherms under lower partial pressure (0-0.25 P/P_o) (**Figure S18**).

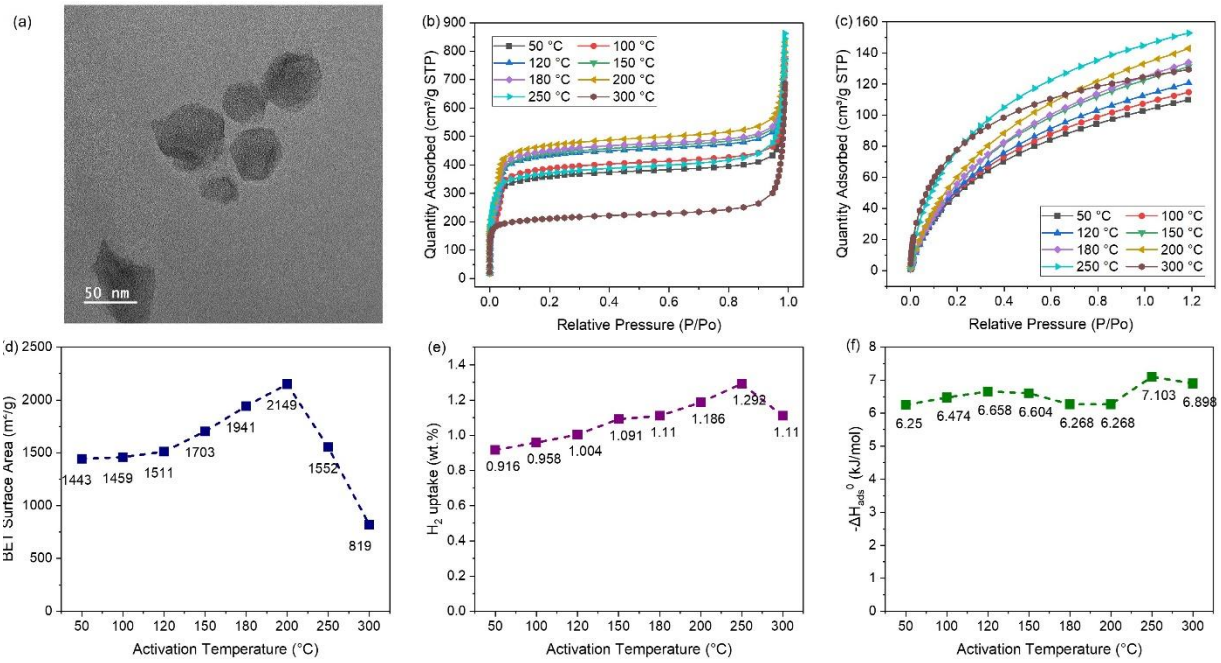

Figure 6 (a) TEM image, (b) N_2 adsorption isotherms at 77 K, and c) H_2 adsorption isotherms at 77 K up to 1 bar for MOF-808@Mg2:1; Summaries of BET surface areas (d), wt.% H_2 adsorbed at 1 bar/77K (e), and the heat of adsorption ($-\Delta H_{ads}^0$) (f) of post-synthetically Mg-doped MOF-808@Mg2:1 activated at various temperatures.

Furthermore, MOF-808@Mg2:1 showed excellent stability under ambient conditions and in aqueous solutions, evidenced by PXRD (**Figure S19**) and gas sorption studies (**Figure S20**). After exposing to air for two weeks, MOF-808@Mg2:1 was re-activated at 200 °C, which exhibited a BET surface area of 1,925 m^2/g, H_2 uptake of 1.14 % and heat of adsorption ($-\Delta H_{ads}^0$) of 5.913 kJ/mol (**Figure S20**). MOF-808@Mg2:1 post air exposure retained most of its porosity and H_2 adsorption capacity compared to the pristine MOF-808 (BET surface area of 2,149 m^2/g, H_2 uptake of 1.19 wt.%, and heat of adsorption $-\Delta H_{ads}^0$ of 6.268 kJ/mol). Our results demonstrate that Mg-doped MOF-808 obtained via post-synthetic modification not only achieved simultaneous enhancement in H_2 uptake and H_2 affinity (heat of adsorption), but it also retained the excellent

stability of MOF-808. We also conducted five consecutive hydrogen adsorption-desorption cycles for MOF-808@Mg 2:1 at 77 K (**Figure S21**), and the results showed that the H_2 uptake remained consistent up to 1.2 bar. Notably, no activation was required between each cycle, suggesting fully reversible H_2 adsorption-desorption cycles occurred in MOF-808@Mg2:1.

Figure 7 summarizes the increase in surface area, H_2 uptake, and heat of adsorption for MOF-808-ZrCu and MOF-808@Mg2:1 compared to the pristine MOF-808. Overall, MOF-808-ZrCu exhibited the highest enhancement in heat of adsorption ($-\Delta H_{ads}^0$) for H_2, even though its BET surface area and H_2 uptake are generally lower than those of pristine MOF-808 (**Figure 7**a and **Figure S22**). Notably, MOF-808-ZrCu activated at 300 °C showed the highest heat of adsorption ($-\Delta H_{ads}^0$) for H_2 (7.686 kJ/mol) among all samples, achieving a 33% enhancement compared to pristine MOF-808 activated at the same temperature; however, MOF-808-ZrCu also exhibited the lowest H_2 uptake among all samples when activated at 300 °C due to the framework collapse and loss of porosity (**Figure S22**ac). On the other hand, MOF-808@Mg2:1 not only showed a higher heat of adsorption ($-\Delta H_{ads}^0$) consistently across various activation temperatures compared to pristine MOF-808, but it also adsorbed more H_2 relative to pristine MOF-808 when activated at or above 200 °C (**Figure 7**b). In particular, when the activation temperature increased to 250 °C, the heat of adsorption ($-\Delta H_{ads}^0$) and H_2 uptake of MOF-808@Mg2:1 both increased remarkably due to the simultaneous generation of Mg and Zr open metal sites. Among all samples, MOF-808@Mg2:1 activated at 250 °C exhibited the highest H_2 uptake of 1.30 wt.% (at 77 K, 1 bar) due to the enrichment of open metal sites by metal doping (**Figure S22**c). Surprisingly, even at 300 °C, MOF-808@Mg2:1 retained decent hydrogen adsorption capacity despite partial structural degradation, showing a 59% higher H_2 uptake than the pristine MOF-808 activated at the same temperature (**Figure 7**b). Overall, our systematic studies showed, for the first time, that metal

doping in Zr-MOFs is an effective strategy to enhance the MOF-H_2 interaction in stable MOFs. In particular, post-synthetic Mg-doping in Zr-MOFs is a promising approach to increase both H_2 uptake and H_2 interaction while maintaining the robustness of Zr-MOFs.

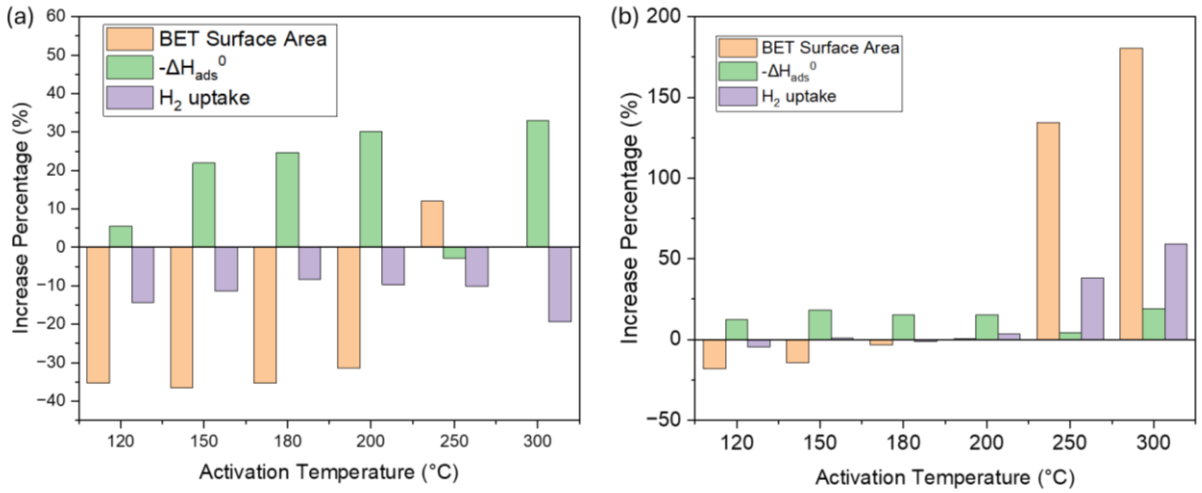

Figure 7 Summaries of the increase percentage in the BET surface area, heat of adsorption ($-\Delta H_{ads}^0$), and H_2 uptake of (a) one-pot Cu-doped MOF-808-ZrCu and (b) post-synthetic Mg-doped MOF-808@Mg2:1 compared to pristine MOF-808 activated at various temperatures.

We then compared the performance of our metal-doped MOFs to representative MOFs in the literature. Since literature-reported H_2 uptake and heat of adsorption values for these representative MOFs vary from study to study, for consistency, we synthesized three previously reported MOFs with open Mg/Cu sites, including Mg-MOF-74, Cu-MOF-74, and HKUST-1, following procedures established in published literature.[41-43] The MOF structures were confirmed with PXRD (**Figure S23**). Their H_2 uptake and heat of adsorption ($-\Delta H_{ads}^0$) were measured and calculated (**Figure S24-S26**).

As summarized in **Table S8**, our MOF-808-ZrCu exhibited a higher heat of adsorption than the two representative Cu-MOFs: HKUST-1 and MOF-74-Cu. Even though our MOF-808@Mg2:1 showed lower heat of adsorption than MOF-74-Mg, its heat of adsorption and total H_2 uptake at 1

bar/77 K are still higher than those of Cu-MOF-74. It is worth noting that, compared to Cu-MOFs and Mg-MOFs with highly concentrated open sites, like those listed in **Table S8**, our metal-doped MOF-808 has a much lower amount of Mg^{2+} or Cu^{2+} in its metal clusters, significantly improving their stability under ambient conditions. As previously mentioned, the H_2 adsorption capacity and heat of adsorption for MOF-808-ZrCu and MOF-808@Mg were retained after storing the samples under ambient conditions for two weeks to a month. In contrast, Mg-MOF-74, Cu-MOF-74, and HKUST-1 are very sensitive to moisture and must be handled carefully under air/moisture-free conditions. In our hands, the gas sorption for these three samples (Mg-MOF-74, Cu-MOF-74, and HKUST-1) dropped significantly even after a brief exposure to the air. Compared to traditional MOFs that are well known for their open metal sites but poor stability, our metal-doped Zr-MOFs with superior stability and reusability hold significant advantages.

DFT investigation of H_2 affinity in pristine and Mg-doped MOF-808

Figure 7 indicates that increasing the activation temperature generally enhances hydrogen uptake in MOF-808. However, its effects on BET surface area and ΔH_{ads}^{0} differ between undoped and Mg-doped samples. To better understand the underlying mechanisms, we performed DFT calculations to assess how temperature-induced water desorption from metal sites influences H_2 interactions in both undoped and Mg-doped MOF-808. In the Mg-doped model, one Zr^{4+} was replaced by Mg^{2+}, accompanied by the conversion of one –OH group to H_2O and one bridging –O– to –OH, resulting in a neutral framework composed of 5 Zr^{4+} and 1 Mg^{2+}.

As shown in **Figure 8**a, Mg dopants exhibit significantly lower water desorption energy compared to pristine Zr sites, suggesting that Mg doping facilitates the formation of reactive open metal sites at lower activation temperatures. We then calculated H_2 binding energies on both hydrated and water-desorbed Zr and Mg sites (**Figure 8**b). For Zr, desorbing two H_2O molecules

does not significantly enhance H_2 binding, likely because water removal triggers substantial Zr–O coordination rearrangements that preserve a 6-fold (closed) coordination geometry. Consequently, the Zr–H_2 distance remains largely unchanged. In contrast, Mg sites undergo a coordination change from 6-fold to 5-fold upon water desorption, enabling stronger H_2 binding. This is evidenced by both a shorter Mg–H_2 distance and a more exothermic binding energy.

Together, these results suggest that the impact of activation temperature diverges for undoped and Mg-doped MOF-808. In undoped samples, water is more strongly bound, and only weakly adsorbed species are removed at lower temperatures, which increases BET surface area and enhances H_2 uptake. In Mg-doped samples, water desorption from Mg sites occurs more readily, even at lower temperatures, leading to the formation of open sites with stronger H_2 interactions. The combination of these stronger Mg–H_2 interactions and a moderately increased surface area results in improved H_2 uptake in Mg-doped MOF-808.

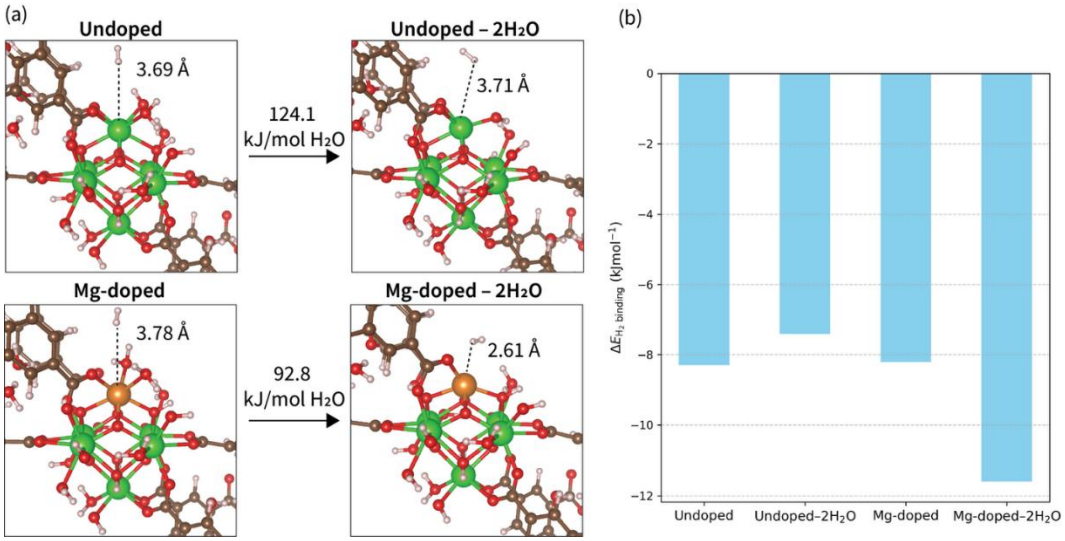

Figure 8 (a) DFT-optimized structures of H_2-adsorbed pristine and Mg-doped MOF-808, with and without H_2O desorption at the Zr/Mg site. (b) DFT-calculated H_2 binding energies at the corresponding four Zr/Mg sites. Atom color scheme: brown – C, red – O, pink – H, green – Zr, orange – Mg.

Conclusions

In summary, various divalent metal ions were incorporated into MOF-808 using one-pot and post-synthetic modification methods. The metal-doped Zr-MOFs generally exhibited enhanced interaction with H_2, owing to the incorporated open metal sites. Remarkably, a Mg-doped MOF, MOF-808@Mg2:1, showed a 59% increase in hydrogen uptake, and a Cu-doped MOF, MOF-808-ZrCu, exhibited a 33% increase in isosteric heat of adsorption ($-\Delta H_{ads}^0$) for H_2 compared to the pristine MOF-808 activated at the same temperature. In addition, the Mg-doped MOF-808@Mg2:1 obtained via post-synthetic modification showed a simultaneous enhancement in both H_2 uptake and H_2 interaction while retaining the excellent stability of MOF-808. DFT calculations revealed that these enhancements were attributed to the easily generated divalent open metal sites integrated into the Zr_6 clusters of the Zr-MOF. This work presents a viable strategy to create highly stable MOFs enriched with easily generated open metal sites for enhanced H_2 adsorption. It demonstrates the potential of metal-doped Zr-MOFs in practical hydrogen storage by balancing material stability and strong affinity for hydrogen.

ASSOCIATED CONTENT

Supporting Information

The Supporting Information is available free of charge on the ACS Publications website at DOI:

PXRD patterns, SEM images, ICP results, FT-IR spectra, and TGA data for all samples, XPS and H_2 adsorption-desorption cycling data for MOF-808@Mg2:1, synthesis procedures for HKUST-1, Cu-MOF-74, and Mg-MOF-74, tables summarizing properties of different samples, as well as comparison between representative MOFs and metal-doped MOF-808.

Notes

The authors declare no competing financial interest.

ACKNOWLEDGMENTS

This work is supported by the U.S. Department of Energy's Office of Energy Efficiency and Renewable Energy (EERE) under the Office of Fossil Energy and Carbon Management, Award No. DE-EE0010430. Y.L. and L.Q. also acknowledge support from the U.S. Department of Energy, Office of Science, Office of Basic Energy Sciences, Materials Chemistry Program, under Award No. DE-SC0024498. S.L. and B.C.W acknowledge support from the Hydrogen Materials Advanced Research Consortium (HyMARC), established as part of the Energy Materials Network by the U.S. Department of Energy (DOE) under Contract DE-AC52-07NA27344, Office of Energy Efficiency and Renewable Energy (EERE), Hydrogen and Fuel Cell Technologies Office. Part of this work was performed under the auspices of the DOE by Lawrence Livermore National Laboratory under Contract No. DE-AC52-07NA27344. The computational portion of this research was performed using computational resources sponsored by the Department of Energy's Office of Energy Efficiency and Renewable Energy and located at the National Renewable Energy Laboratory. The authors acknowledge Dr. Varun Raviprolu from UCLA for his support in maintaining the ICP-OES instrument and ensuring its proper operation during data acquisition.

REFERENCES

1. Zhang, J.; Bai, T.; Huang, H.; Yu, M.-H.; Fan, X.; Chang, Z.; Bu, X.-H., Metal–Organic-Framework-Based Photocatalysts Optimized by Spatially Separated Cocatalysts for Overall Water Splitting. *Adv. Mater.* 2020, *32* (49), 2004747.

2. Roy, S.; Huang, Z.; Bhunia, A.; Castner, A.; Gupta, A. K.; Zou, X.; Ott, S., Electrocatalytic Hydrogen Evolution from a Cobaloxime-Based Metal–Organic Framework Thin Film. *J. Am. Chem. Soc.* 2019, *141* (40), 15942-15950.

3. Ren, J.; Langmi, H. W.; North, B. C.; Mathe, M., Review on processing of metal–organic framework (MOF) materials towards system integration for hydrogen storage. *Int. J. Energy Res.* 2015, *39* (5), 607-620.

4. Sculley, J.; Yuan, D.; Zhou, H.-C., The current status of hydrogen storage in metal–organic frameworks—updated. *Energy Environ. Sci.* 2011, *4* (8), 2721-2735.

5. Xie, Z.; Jin, Q.; Su, G.; Lu, W. A Review of Hydrogen Storage and Transportation: Progresses and Challenges *Energies* [Online], 2024.

6. Shet, S. P.; Shanmuga Priya, S.; Sudhakar, K.; Tahir, M., A review on current trends in potential use of metal-organic framework for hydrogen storage. *Int. J. Hydrogen Energy.* 2021, *46* (21), 11782-11803.

7. Li, J.-R.; Kuppler, R.; Zhou, H.-C., Selective Gas Adsorption and Separation in Metal-Organic Frameworks. *Chem. Soc. Rev.* 2009, *38*, 1477-504.

8. Oh, C.; Nandy, A.; Yue, S.; Kulik, H. J., MOFs with the Stability for Practical Gas Adsorption Applications Require New Design Rules. *ACS Appl. Mater. Interfaces* 2024, *16* (41), 55541-55554.

9. Zhou, D.; Zheng, C.; Zhang, Y.; Sun, H.; Sheng, P.; Zhang, X.; Li, J.; Guo, S.; Zhao, D., An overview of RE-Mg-based alloys for hydrogen storage: Structure, properties, progresses and perspectives. *J. Magnes. Alloy* 2025, *13* (1), 41-70.

10. Li, S.; Zhang, L.; Wu, F.; Jiang, Y.; Yu, X., Efficient catalysis of FeNiCu-based multi-site alloys on magnesium-hydride for solid-state hydrogen storage. *Chin. Chem. Lett.* 2025, *36* (1), 109566.

11. Song, M.-C.; Wu, F.-Y.; Jiang, Y.-Q.; Wang, X.-Z.; Zhao, H.; Chen, L.-X.; Zhang, L.-T., Optimizing FeCoNiCrTi high-entropy alloy with hydrogen pumping effect to boost de/hydrogenation performance of magnesium hydride. *Rare Met.* 2024, *43* (7), 3273-3285.

12. Zhong, T.; Xu, T.; Zhang, L.; Wang, L.; Wu, F.; Yu, X., Modulation on Surface Termination Groups to Optimize the Adsorption Energy and Work Function of Nb2CTx for Enhanced Hydrogen Storage in Magnesium Hydride. *Adv. Funct. Mater.* 2025, *35* (13), 2418230.

13. Zhong, T.; Xu, T.; Zhang, L.; Wu, F.; Jiang, Y.; Yu, X., Designing multivalent NiMn-based layered nanosheets with high specific surface area and abundant active sites for solid-state hydrogen storage in magnesium hydride. *J. Magnes. Alloy.* 2025, *13* (1), 148-160.

14. García Blanco, A. A.; Vallone, A. F.; Korili, S. A.; Gil, A.; Sapag, K., A comparative study of several microporous materials to store methane by adsorption. *Micropor. Mesopor. Mat.* 2016, *224*, 323-331.

15. Hassan, I. A.; Ramadan, H. S.; Saleh, M. A.; Hissel, D., Hydrogen storage technologies for stationary and mobile applications: Review, analysis and perspectives. *Renew. Sustain. Energy Rev.* 2021, *149*, 111311.

16. Ströbel, R.; Garche, J.; Moseley, P. T.; Jörissen, L.; Wolf, G., Hydrogen storage by carbon materials. *J. Power Sources* 2006, *159* (2), 781-801.

17. Li, B.; Wen, H.-M.; Zhou, W.; Xu, Jeff Q.; Chen, B., Porous Metal-Organic Frameworks: Promising Materials for Methane Storage. *Chem* 2016, *1* (4), 557-580.

18. Jiang, C.; Wang, X.; Ouyang, Y.; Lu, K.; Jiang, W.; Xu, H.; Wei, X.; Wang, Z.; Dai, F.; Sun, D., Recent advances in metal–organic frameworks for gas adsorption/separation. *Nanoscale Adv.* 2022, *4* (9), 2077-2089.

19. Sun, Y.; Wang, L.; Amer, W. A.; Yu, H.; Ji, J.; Huang, L.; Shan, J.; Tong, R., Hydrogen Storage in Metal-Organic Frameworks. *J. Inorg. Organomet. Polym. Mater.* 2013, *23* (2), 270-285.

20. Allendorf, M. D.; Hulvey, Z.; Gennett, T.; Ahmed, A.; Autrey, T.; Camp, J.; Seon Cho, E.; Furukawa, H.; Haranczyk, M.; Head-Gordon, M.; Jeong, S.; Karkamkar, A.; Liu, D.-J.; Long, J. R.; Meihaus, K. R.; Nayyar, I. H.; Nazarov, R.; Siegel, D. J.; Stavila, V.; Urban, J. J.; Veccham, S. P.; Wood, B. C., An assessment of strategies for the development of solid-state adsorbents for vehicular hydrogen storage. *Energy Environ. Sci.* 2018, *11* (10), 2784-2812.

21. Jaramillo, D. E.; Jiang, H. Z. H.; Evans, H. A.; Chakraborty, R.; Furukawa, H.; Brown, C. M.; Head-Gordon, M.; Long, J. R., Ambient-Temperature Hydrogen Storage via Vanadium(II)-Dihydrogen Complexation in a Metal–Organic Framework. *J. Am. Chem. Soc.* 2021, *143* (16), 6248-6256.

22. Sengupta, D.; Melix, P.; Bose, S.; Duncan, J.; Wang, X.; Mian, M. R.; Kirlikovali, K. O.; Joodaki, F.; Islamoglu, T.; Yildirim, T.; Snurr, R. Q.; Farha, O. K., Air-Stable Cu(I) Metal–Organic Framework for Hydrogen Storage. *J. Am. Chem. Soc.* 2023, *145* (37), 20492-20502.

23. Kim, D. W.; Jung, M.; Shin, D. Y.; Kim, N.; Park, J.; Lee, J.-H.; Oh, H.; Hong, C. S., Fine-tuned MOF-74 type variants with open metal sites for high volumetric hydrogen storage at near-ambient temperature. *Chem. Eng. J.* 2024, *489*, 151500.

24. Nowotny, J.; Veziroglu, T. N., Impact of hydrogen on the environment. *Int. J. Hydrogen Energy* 2011, *36* (20), 13218-13224.

25. Liu, Y.-L.; Zhao, Y.; Zhang, J.; Ye, Y.; Sun, Q., Cu2-cluster-based MOF with open metal sites and Lewis basic sites: Construction, CO2 adsorption and fixation. *J. Solid State Chem.* 2022, *313*, 123332.

26. Yan, Y.; Yang, S.; Blake, A. J.; Schröder, M., Studies on Metal–Organic Frameworks of Cu(II) with Isophthalate Linkers for Hydrogen Storage. *Acc. Chem. Res.* 2014, *47* (2), 296-307.

27. Sumida, K.; Rogow, D. L.; Mason, J. A.; McDonald, T. M.; Bloch, E. D.; Herm, Z. R.; Bae, T.-H.; Long, J. R., Carbon Dioxide Capture in Metal–Organic Frameworks. *Chem. Rev.* 2012, *112* (2), 724-781.

28. Cavka, J. H.; Jakobsen, S.; Olsbye, U.; Guillou, N.; Lamberti, C.; Bordiga, S.; Lillerud, K. P., A New Zirconium Inorganic Building Brick Forming Metal Organic Frameworks with Exceptional Stability. *J. Am. Chem. Soc.* 2008, *130* (42), 13850-13851.

29. Yuan, S.; Peng, J.; Zhang, Y.; Shao-Horn, Y., Stability Trend of Metal–Organic Frameworks with Heterometal-Modified Hexanuclear Zr Building Units. *J. Phys. Chem. C.* 2019, *123* (46), 28266-28274.

30. Hou, X.; Jin, L.; Wang, C.; Gu, L.; Li, J.; Yang, L., Non-Noble Metal-Doped MOF-808-Zr Nanostructures with Abundant Defects for Toluene Oxidation. *ACS Appl. Nano Mater.* 2023, *6* (19), 17397-17405.

31. Gil-San-Millan, R.; López-Maya, E.; Platero-Prats, A. E.; Torres-Pérez, V.; Delgado, P.; Augustyniak, A. W.; Kim, M. K.; Lee, H. W.; Ryu, S. G.; Navarro, J. A. R., Magnesium

Exchanged Zirconium Metal–Organic Frameworks with Improved Detoxification Properties of Nerve Agents. *J. Am. Chem. Soc.* 2019, *141* (30), 11801-11805.

32. Ding, M.; Cai, X.; Jiang, H.-L., Improving MOF stability: approaches and applications. *Chem. Sci.* 2019, *10* (44), 10209-10230.

33. Dai, S.; Simms, C.; Dovgaliuk, I.; Patriarche, G.; Tissot, A.; Parac-Vogt, T. N.; Serre, C., Monodispersed MOF-808 Nanocrystals Synthesized via a Scalable Room-Temperature Approach for Efficient Heterogeneous Peptide Bond Hydrolysis. *Chem. Mater.* 2021, *33* (17), 7057-7066.

34. Nuhnen, A.; Janiak, C., A practical guide to calculate the isosteric heat/enthalpy of adsorption via adsorption isotherms in metal–organic frameworks, MOFs. *Dalton Trans.* 2020, *49* (30), 10295-10307.

35. Kresse, G.; Furthmüller, J., Efficient iterative schemes for ab initio total-energy calculations using a plane-wave basis set. *Phys. Rev. B* 1996, *54* (16), 11169-11186.

36. Kresse, G.; Joubert, D., From ultrasoft pseudopotentials to the projector augmented-wave method. *Phys. Rev. B* 1999, *59* (3), 1758-1775.

37. Blöchl, P. E., Projector augmented-wave method. *Phys. Rev. B* 1994, *50* (24), 17953-17979.

38. Hamada, I., van der Waals density functional made accurate. *Phys. Rev. B* 2014, *89* (12), 121103.

39. Vlaisavljevich, B.; Huck, J.; Hulvey, Z.; Lee, K.; Mason, J. A.; Neaton, J. B.; Long, J. R.; Brown, C. M.; Alfè, D.; Michaelides, A.; Smit, B., Performance of van der Waals Corrected

Functionals for Guest Adsorption in the M2(dobdc) Metal–Organic Frameworks. *J. Phys. Chem. A* 2017, *121* (21), 4139-4151.

40. Yang, B.; Wheeler, J. I.; Sorensen, B.; Steagall, R.; Nielson, T.; Yao, J.; Mendez-Arroyo, J.; Ess, D. H., Computational determination of coordination structure impact on adsorption and acidity of pristine and sulfated MOF-808. *Mater. Adv.* 2021, *2* (13), 4246-4254.

41. Al-Naddaf, Q.; Rezaei, F., Multicomponent adsorptive separation of CO2, CO, CH4, N2, and H2 over core-shell zeolite-5A@MOF-74 composite adsorbents. *Chem. Eng. J.* 2019, *384*, 123251.

42. Rosnes, M. H.; Opitz, M.; Frontzek, M.; Lohstroh, W.; Embs, J. P.; Georgiev, P. A.; Dietzel, P. D. C., Intriguing differences in hydrogen adsorption in CPO-27 materials induced by metal substitution. *J. Mater. Chem. A* 2015, *3* (9), 4827-4839.

43. Kwon, O.; Kim, J. Y.; Park, S.; Lee, J. H.; Ha, J.; Park, H.; Moon, H. R.; Kim, J., Computer-aided discovery of connected metal-organic frameworks. *Nat. Commun.* 2019, *10* (1), 3620.

TOC Graphic

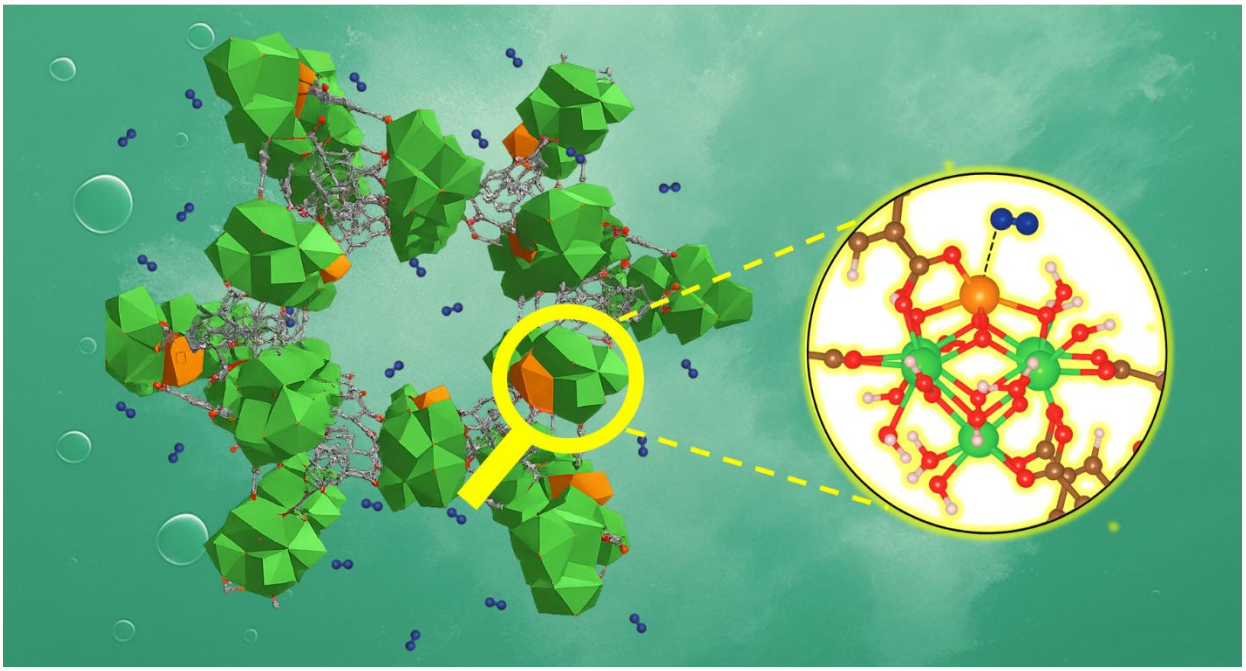

Supporting Information

Enhancing Dihydrogen Interaction of a Zirconium Metal−Organic Framework by Metal Doping

Xiyuan Yao,[a] Sichi Li,[b,c,*], Matthew J. Tang,[a] Hashim Al Khunaizi,[e] Long Qi,[e] Brandon C. Wood,[b,c] and Yangyang Liu[a,*]

[a] Department of Chemistry and Biochemistry, California State University, Los Angeles, 5151 State University Drive, Los Angeles, California 90032, United States

[b] Materials Science Division, Lawrence Livermore National Laboratory, Livermore, California 94550, United States

[c] Laboratory for Energy Applications for the Future (LEAF), Lawrence Livermore National Laboratory, Livermore, California 94550, United States

[d] Department of Chemistry and Biochemistry, University of California, Los Angeles, Los Angeles, California, 90095, United States

[e] U.S. DOE Ames National Laboratory, Iowa State University, Ames, Iowa 50011, United States

[*]Corresponding authors: yliu114@calstatela.edu (Y. L.); li77@llnl.gov (S.L.)

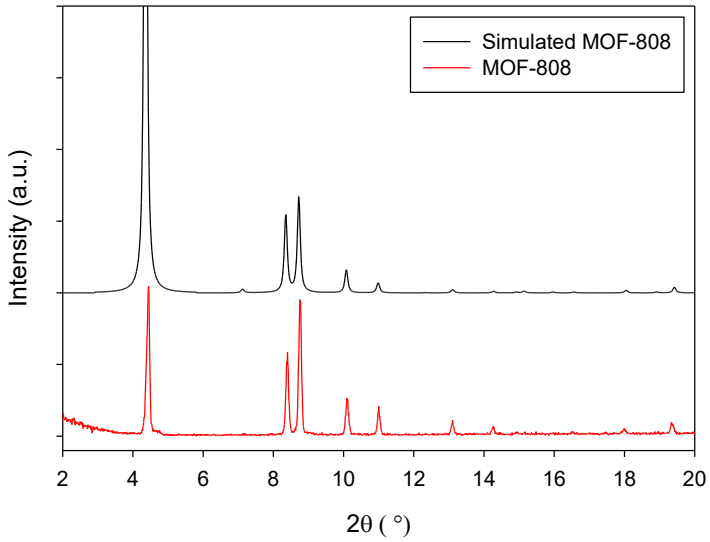

Figure S1 PXRD patterns of simulated and experimental MOF-808

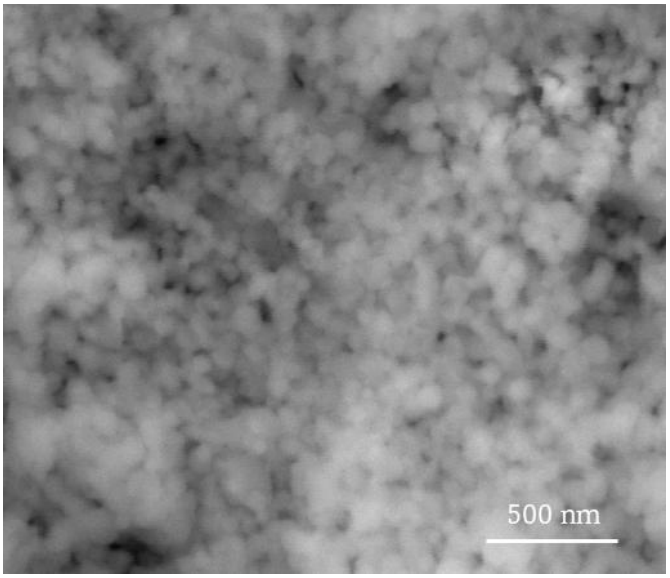

Figure S2 SEM image of the pristine MOF-808

Table S1 BET surface area, pore size, pore volume, wt.% H_2 adsorbed at 1 bar and 77 K, and ΔH_{ads}^0 of pristine MOF-808 activated at different temperature.

Activation Temperature (ºC)	BET Surface Area (m^2/g)	Pore Width (Å)	Incremental Pore Volume (cm^3/g)	H_2 uptake (wt.%)	$-\Delta H_{ads}^0$ (kJ/mol)
180	2060				
50	1443	19.2	0.07	0.957	6.578
100	1745	18.8 22.4	0.11 0.05	1.042	6.39
120	1847	18.8 22.4	0.11 0.06	1.052	5.934
150	1990	18.8 22.4	0.11 0.07	1.083	5.581
180	2010	19.2 22.4	0.11 0.10	1.122	5.438
200	2142	19.2 22.4	0.11 0.12	1.145	5.437
250	662	11.3 14.2	0.03 0.01	0.936	6.82
300	292	13.8	0.02	0.697	5.781

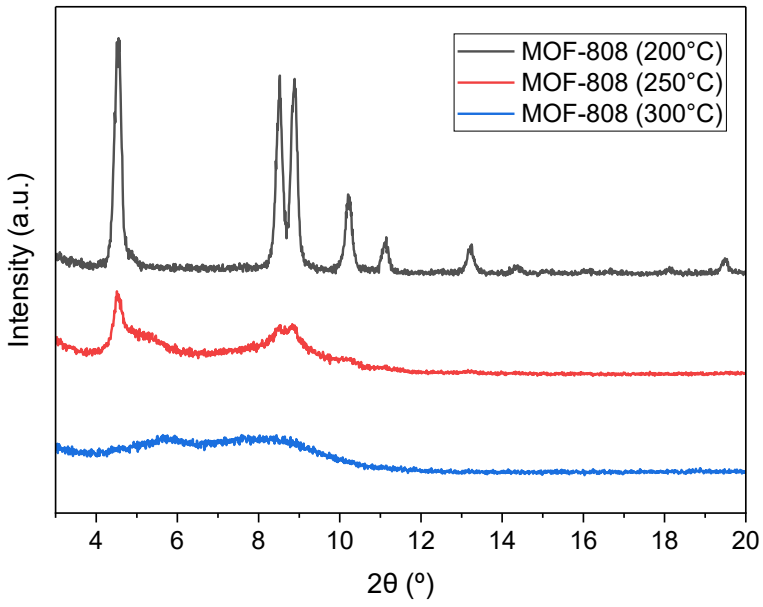

Figure S3 PXRD patterns of pristine MOF-808 activated at 200, 250, and 300 °C.

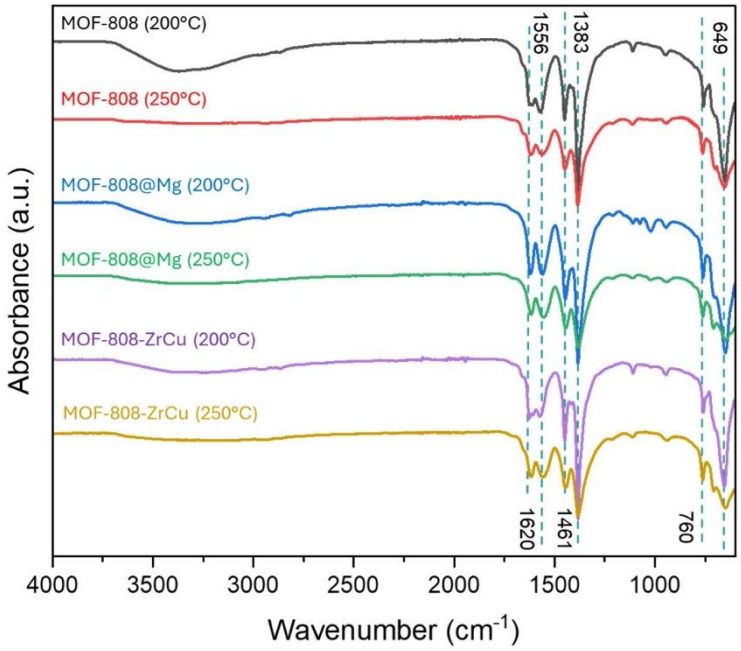

Figure S4 FT-IR spectra of pristine MOF-808, post-synthetic metal-doped MOF-808@Mg2:1, and one-pot metal-doped MOF-808-Cu activated at 200 °C and 250 °C, respectively.

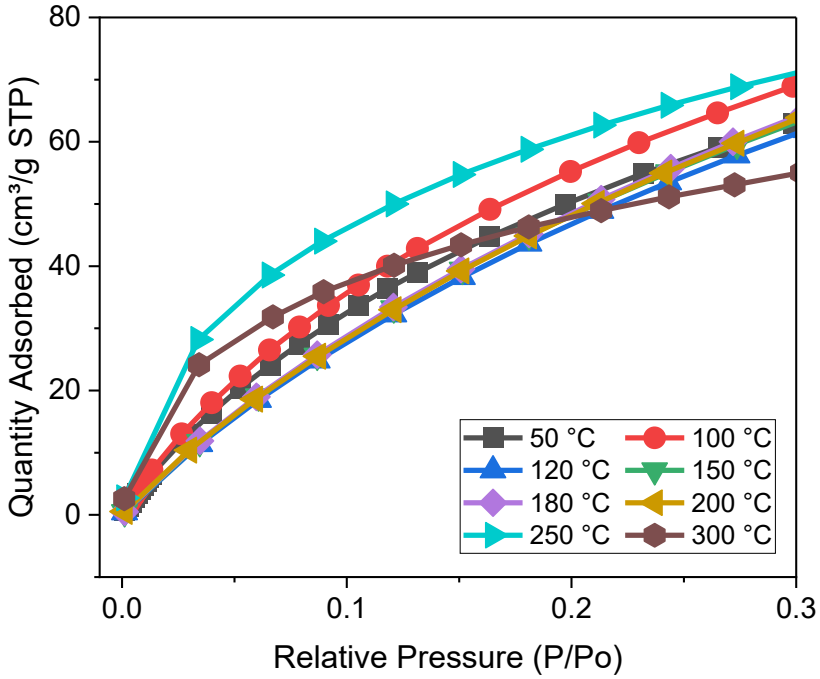

Figure S5 H_2 adsorption isotherms at 77 K up to 0.15 bar of pristine MOF-808 activated at various temperatures.

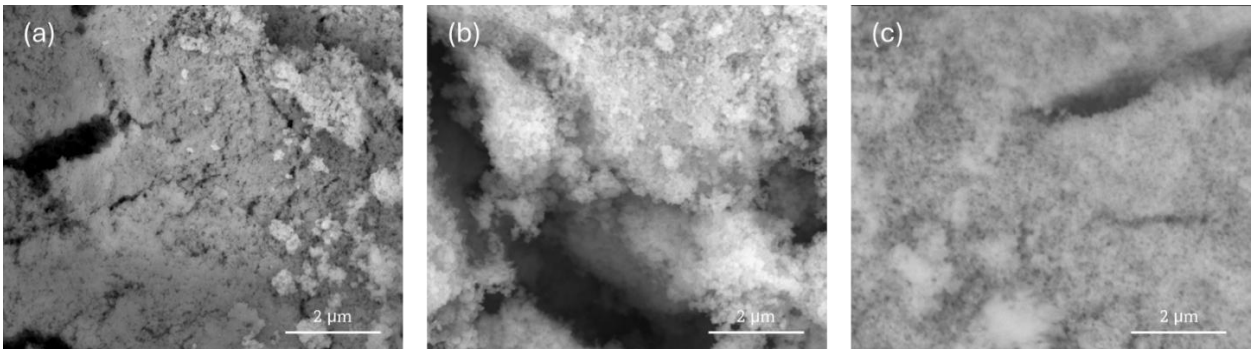

Figure S6 SEM image of the metal-doped MOF-808-ZrM (a) MOF-808-ZrMn, (b) MOF-808-ZrCu and (c) MOF-808-ZrCa.

Table S2 Molar ratio of doped metal to Zr_6 for MOF-808-ZrM from ICP-OES

Molar Ratio	**MOF-808**
Ratio (Mn/Zr_6)	0.13
Ratio (Cu/Zr_6)	0.03
Ratio (Ca/Zr_6)	0.16

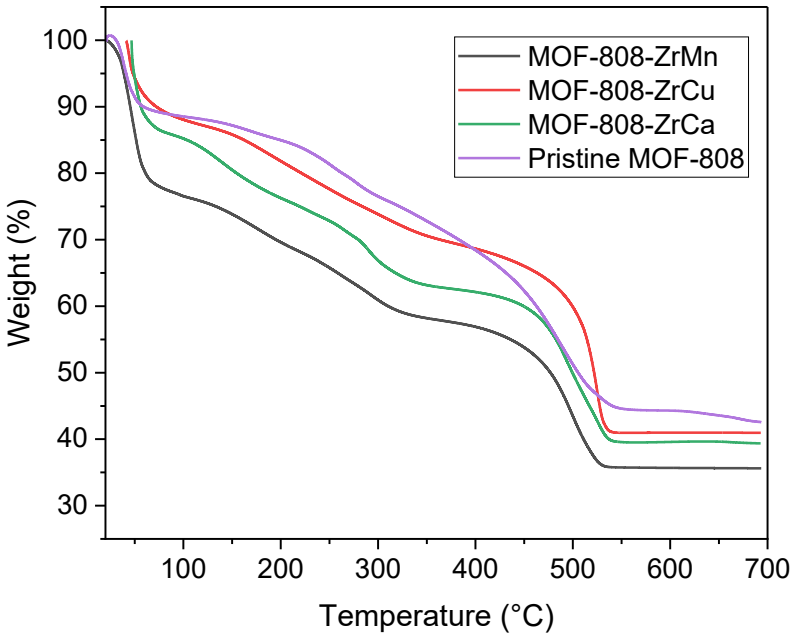

Figure S7 TGA of one-pot metal-doped MOF-808-ZrM (M = Mn, Cu, and Ca).

Table S3 Molar ratio of doped metal ions to Zr_6 cluster calculated based on ICP-OES results, BET surface area, pore size, pore volume, and ΔH_{ads}^{0} of one-pot metal-doped MOF-808-ZrM.

MOF-808	Doped Metal	Ratio (M/Zr_6) from ICP-OES	BET Surface Area (m^2/g)	Pore Width (Å)	Incremental Pore Volume (cm^3/g)	$-\Delta H_{ads}^{0}$ (kJ/mol)
Published			2060			
Pristine MOF-808			1847	18.8 22.4	0.11 0.06	5.934
One-pot Doped MOF-808	Mn	0.13	1470	18.8	0.11	6.422
	Ca	0.16	1798	19.16	0.14	6.244
	Cu	0.03	1195	14.16 18.8	0.04 0.07	6.259

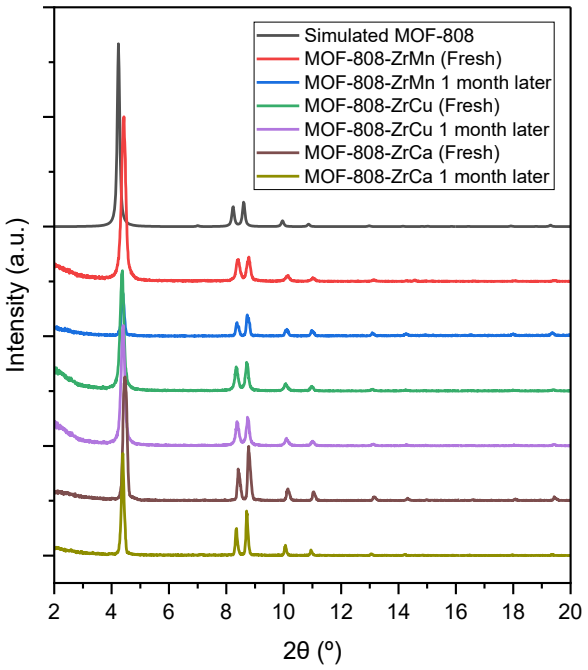

Figure S8 PXRD patterns of one-pot metal-doped MOF-808-ZrM after being stored under ambient conditions for a month.

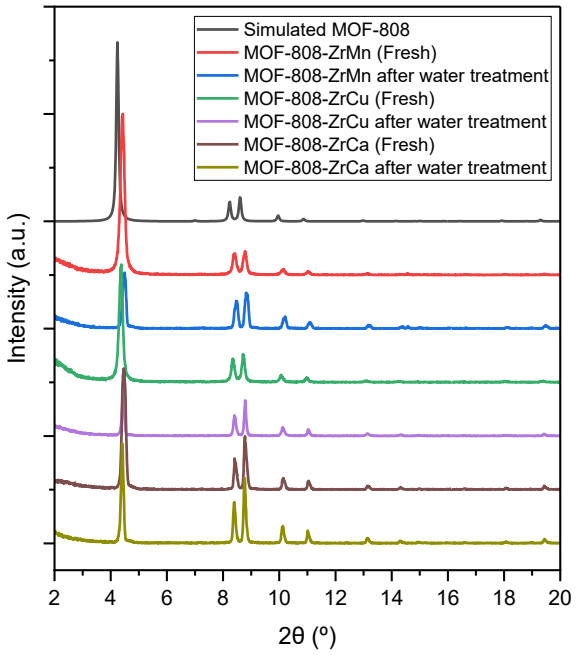

Figure S9 PXRD patterns of one-pot metal-doped MOF-808-ZrM after being stored in an aqueous solution for one week.

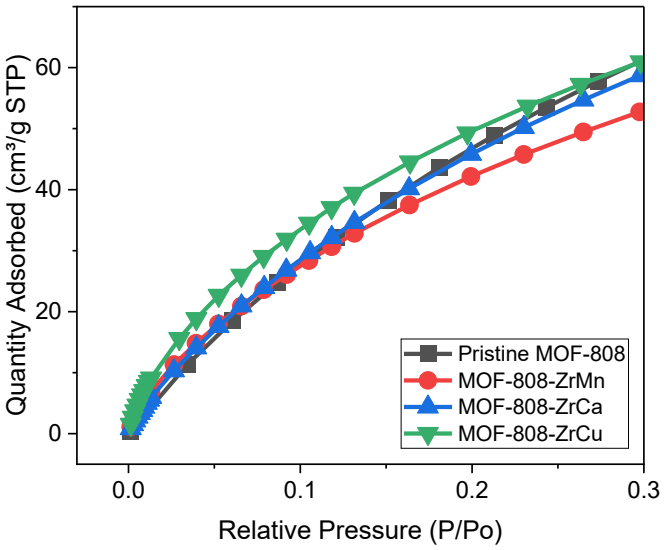

Figure S10 H_2 adsorption isotherms at 77 K up to 0.3 bar of pristine MOF-808 and metal-doped MOF-808-ZrM (M = Mn, Ca, and Cu) obtained through one-pot synthesis.

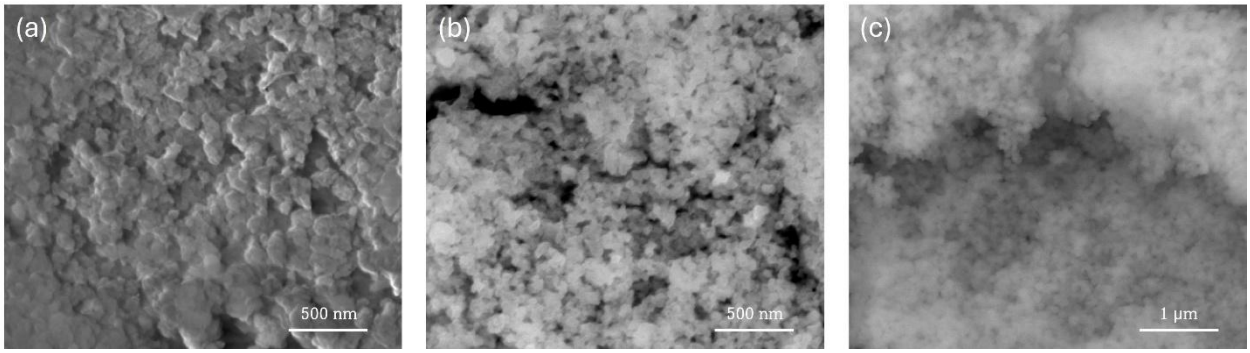

Figure S11 SEM images of the metal-doped MOF-808@Mg (a) MOF-808@Mg1:1, (b) MOF-808@Mg2:1 and (c) MOF-808@Mg3:1.

Table S4 Molar ratio of Mg to Zr_6 cluster for MOF-808@Mg samples calculated from ICP results

MOF-808@Mg	**Ratio (Mg/Zr_6)**
MOF-808@Mg 1:1	0.812
MOF-808@Mg 2:1	0.361
MOF-808@Mg 3:1	0.336

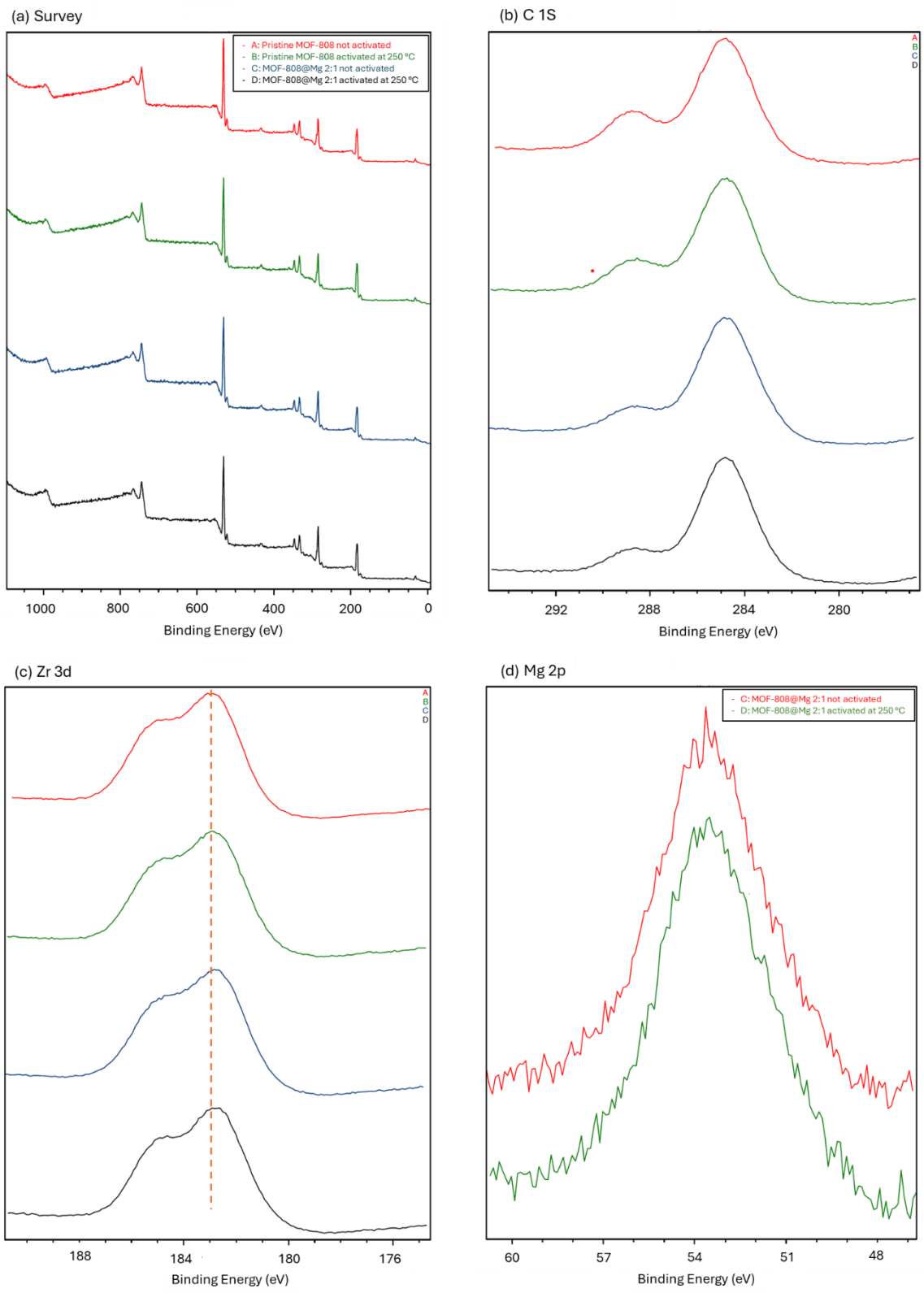

Figure S12 XPS spectra for pristine MOF-808 and post-synthetic metal-doped MOF-808@Mg 2:1, as-synthesized and activated at 250 °C. (a) survey, (b) C 1S, (c) Zr 3d and (d) Mg 2p.

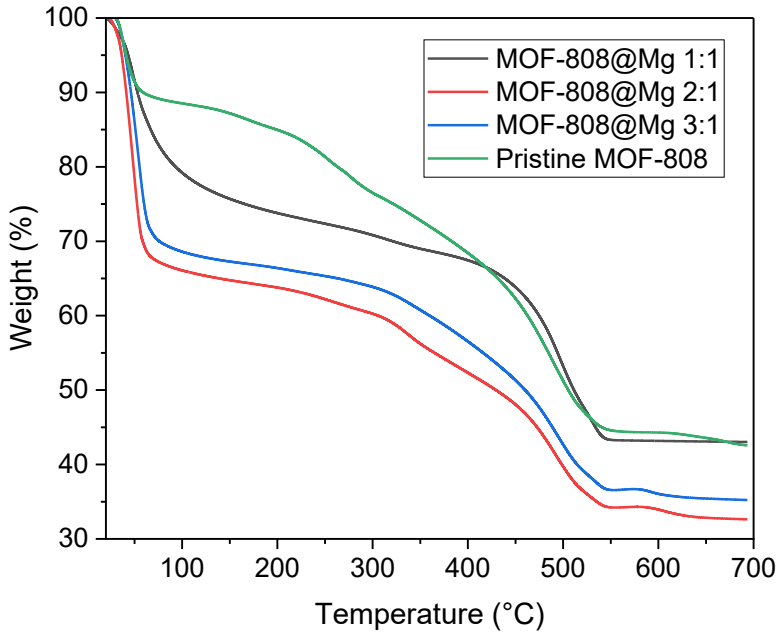

Figure S13 TGA of post-synthetic Mg-doped MOF-808@Mg

Table S5 BET surface area, pore size, pore volume, and $-\Delta H_{ads}^{0}$ of post-synthetic metal-doped MOF-808@Mg.

MOF-808	BET Surface Area (m^2/g)	Pore Width (Å)	Incremental Pore Volume (cm^3/g)	H_2 uptake (wt.%)	$-\Delta H_{ads}^{0}$ (kJ/mol)
MOF-808@Mg 1:1	793	15.23 18.80	0.04 0.02	0.595	5.634
MOF-808@Mg 2:1	1437	18.80 22.38	0.11 0.01	0.916	6.25
MOF-808@Mg 3:1	1548	18.80	0.13	0.922	6.236

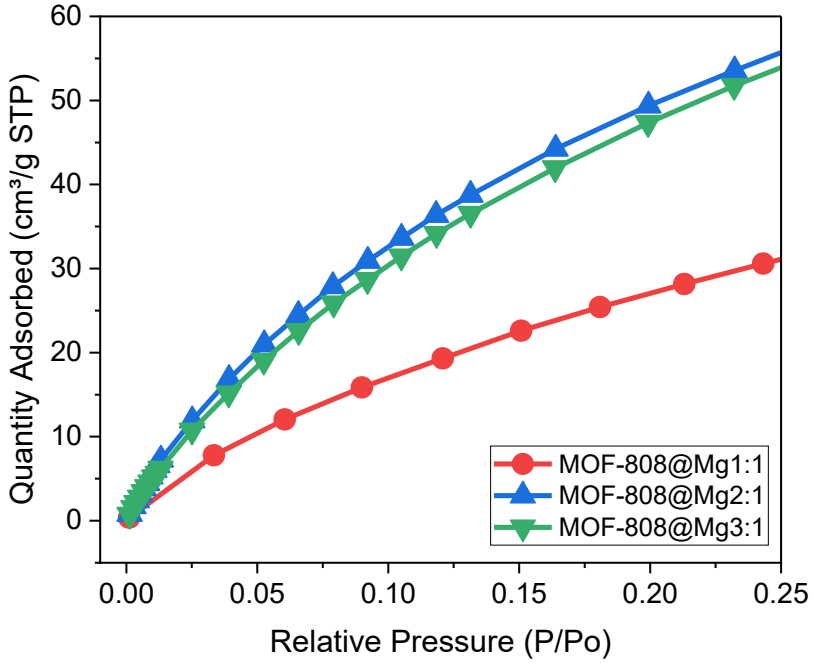

Figure S14 H_2 adsorption isotherms at 77 K up to 0.25 bar of post-synthetic Mg-doped MOF-808@Mg samples.

Table S6 BET surface area, pore size, pore volume, wt.% H_2 adsorbed at 1 bar and $-\Delta H_{ads}^0$ of one-pot metalated MOF-808-ZrCu.

Activation Temperature (°C)	BET Surface Area (m^2/g)	Pore Width (Å)	Incremental Pore Volume (cm^3/g)	H_2 uptake (wt.%)	$-\Delta H_{ads}^0$ (kJ/mol)
120	1195	14.16 18.8	0.04 0.07	0.900	6.259
150	1263	14.16 18.80	0.04 0.09	0.960	6.804
180	1300	14.16 18.80	0.03 0.10	1.029	6.777
200	1469	14.16 18.80	0.04 0.10	1.034	7.074
250	742	11.65 13.80	0.02 0.02	0.841	6.623
300	424	13.80	0.01	0.562	7.686

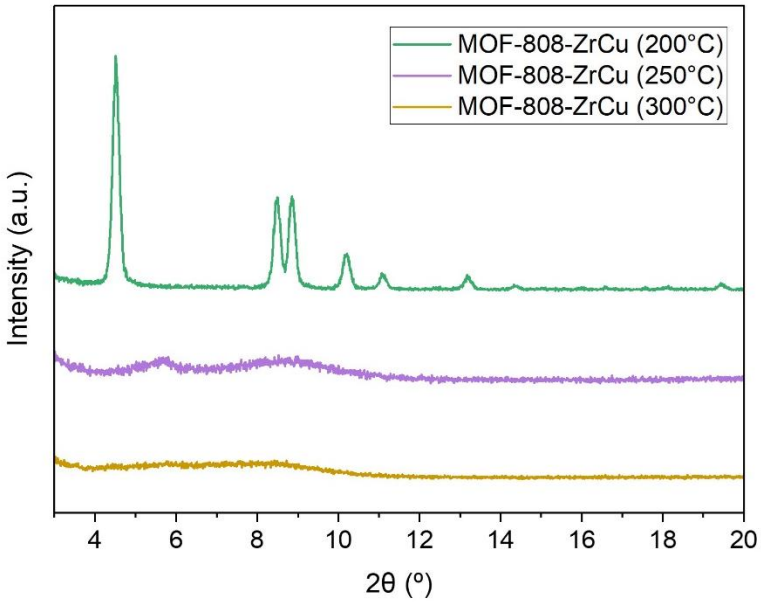

Figure S15 PXRD patterns of MOF-808-ZrCu activated at 200, 250, and 300 °C.

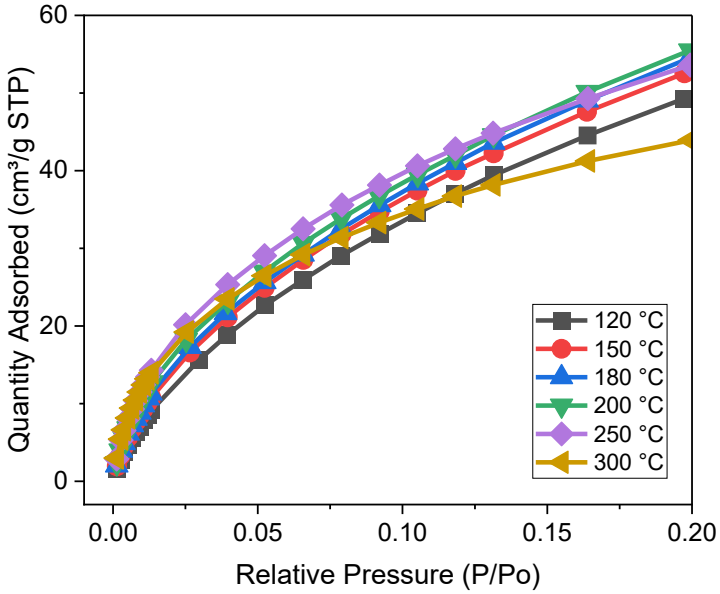

Figure S16 H_2 adsorption isotherms at 77 K up to 0.2 bar of Cu-doped MOF-808-ZrCu activated under different temperatures.

Table S7 BET surface area, pore size, pore volume, wt.% H_2 adsorbed at 1 bar and ΔH_{ads}^0 of post-synthetic metal doped MOF-808@Mg2:1 activated at various temperatures.

Activation Temperature (°C)	BET Surface Area (m^2/g)	Pore Width (Å)	Incremental Pore Volume (cm^3/g)	H_2 uptake (wt.%)	$-\Delta H_{ads}^0$ (kJ/mol)
50	1443	18.80 22.38	0.11 0.01	0.916	6.25
100	1459	18.80 22.38	0.12 0.01	0.958	6.474
120	1511	18.80	0.15	1.004	6.658
150	1703	18.80	0.15	1.091	6.604
180	1941	18.80	0.15	1.110	6.268
200	2149	15.59 18.44	0.02 0.21	1.186	6.268
250	1552	11.30 14.87	0.04 0.06	1.292	7.103
300	819	11.65 13.80	0.02 0.02	1.110	6.898

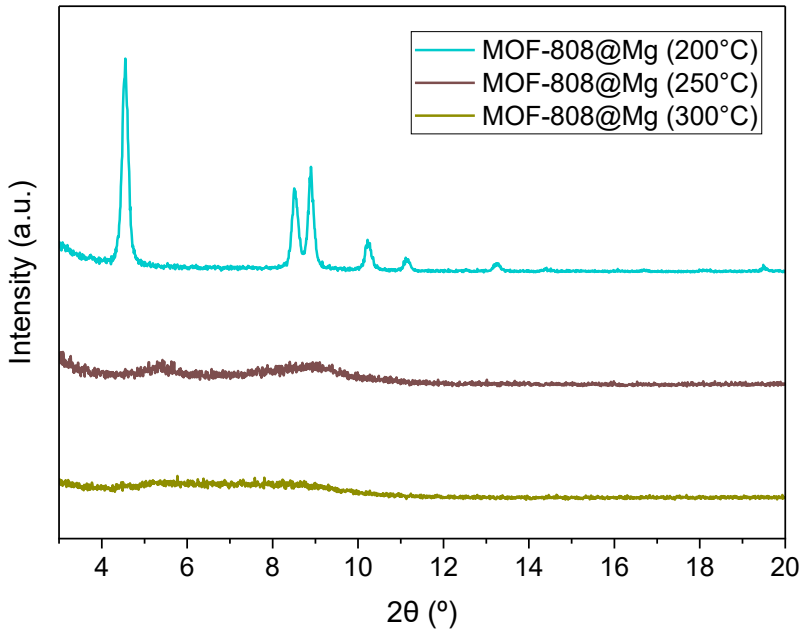

Figure S17 PXRD patterns of MOF-808@Mg 2:1 activated at 200, 250, and 300 °C.

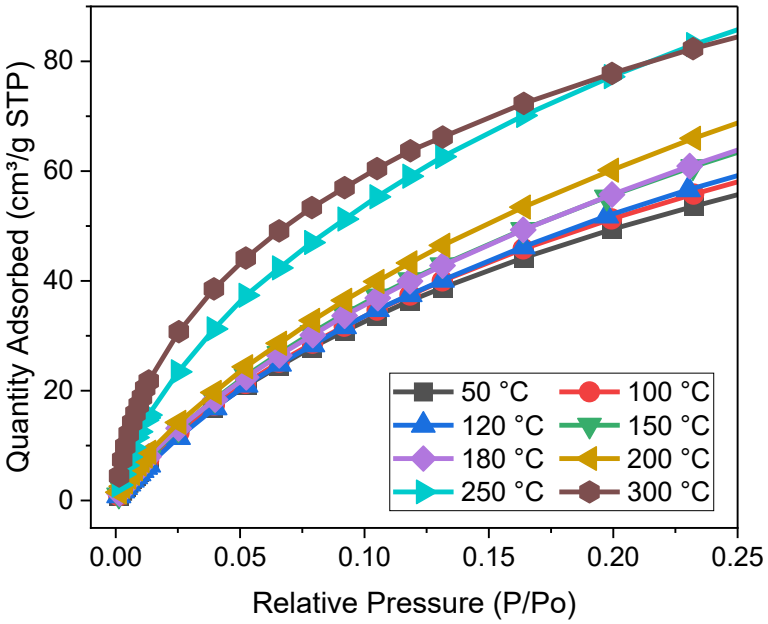

Figure S18 H_2 adsorption isotherms at 77 K up to 0.25 bar of post-synthetically doped MOF-808@Mg2:1 activated at various temperatures.

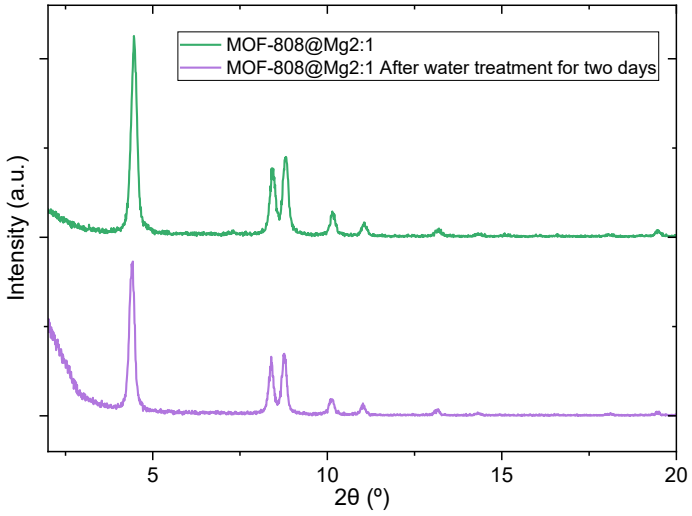

Figure S19 PXRD patterns of post-synthetic Mg-doped MOF-808@Mg2:1 before (green) and after water treatment for two days (purple).

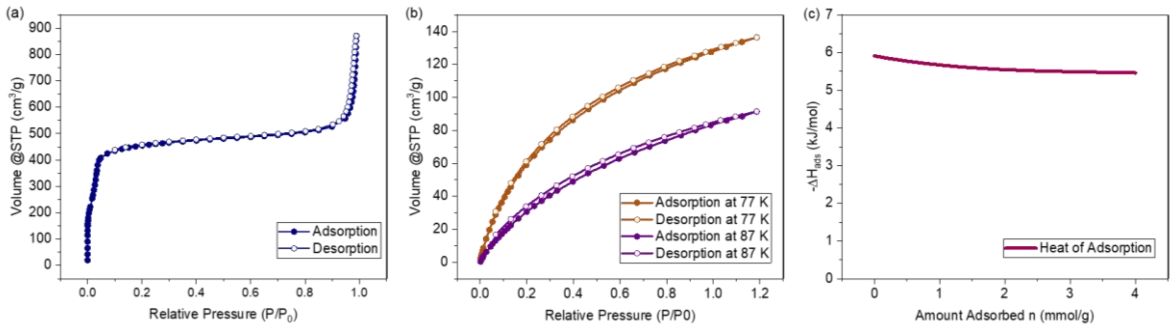

Figure S20 (a) N_2 adsorption isotherm at 77 K, (b) H_2 adsorption isotherm at 77 and 87 K up to 1.2 bar, and (c) heat of adsorption of post-synthetic Mg-doped MOF-808@Mg 2:1 after being stored under ambient conditions for two weeks.

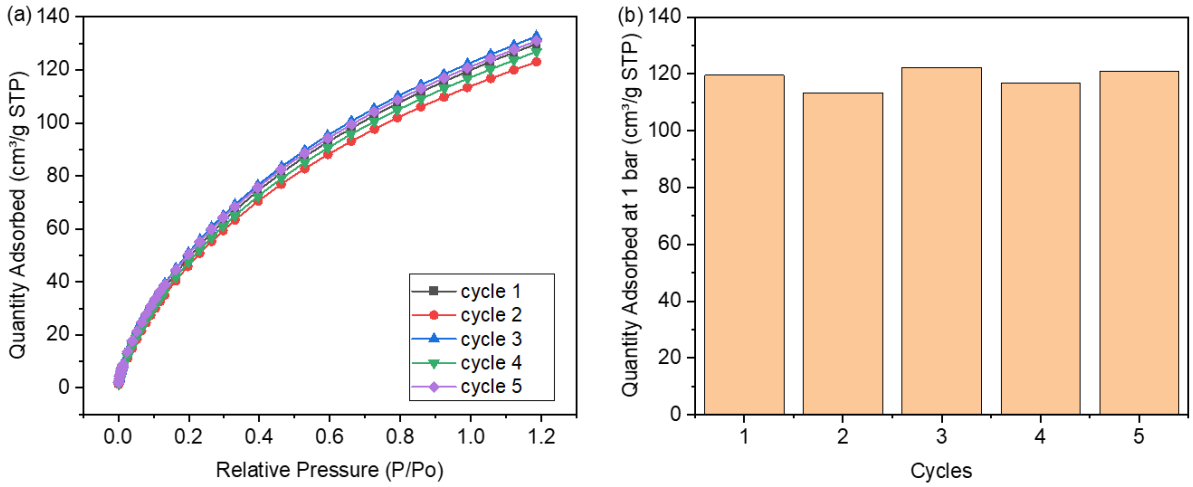

Figure S21 (a) Hydrogen adsorption cycle tests (5 cycles of isotherms at 77 K), (b) H_2 uptake at 1 bar of various cycles.

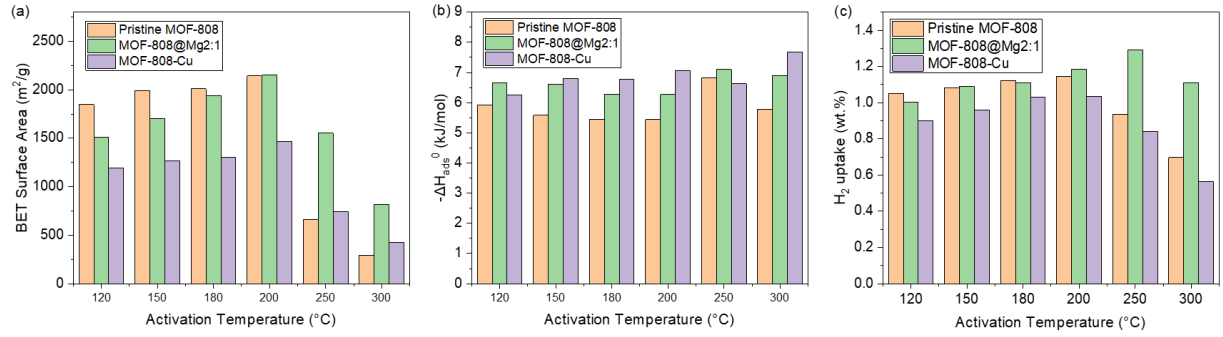

Figure S22 Comparison of (a) BET surface area, (b) heat of adsorption ($-\Delta H_{ads}^{0}$), and (c) H_2 uptake (wt. %) among pristine MOF-808, post-synthetic Mg-doped MOF-808@Mg2:1, and one-pot doped MOF-808-ZrCu.

Synthesis of previously reported Mg and Cu MOFs

Synthesis of Mg-MOF-74

Mg-MOF-74 was synthesized according to the literature with minor modifications.[1] 0.112 g of 2,5-dihydroxyterephthalic acid, 0.475 g $Mg(NO_3)_2 \bullet H_2O$, and 50 mL *N, N'*-dimethylformamide (DMF), ethanol, and H_2O in a 15:1:1 ratio, were added to a 100 mL pressure vessel. The solution was then sonicated for 20 min. The solution was then heated in an oven at 125 °C for 24 h. The product was then washed with DMF 3 times, without centrifuging or shaking, followed by washing with methanol 3 times. Mg-MOF-74 was then activated at 150 °C for 12 h before gas sorption measurements.

Synthesis of Cu-MOF-74

Cu-MOF-74 was synthesized according to the literature with minor modifications.[2] 0.100 g of 2,5-dihydroxyterephthalic acid, 0.235 g $Cu(NO_3)_2 \bullet 2.5H_2O$, 0.028 g DABCO, and 6 mL DMF were added to a 40 mL vial. The solution was then sonicated for 20 min. The solution was then heated in an oven at 60 °C for 3 days. The product was then washed with DMF 3 times, followed by washing with methanol 3 times. Cu-MOF-74 was then activated at 150 °C for 12 h before gas sorption measurements.

Synthesis of HKUST-1

HKUST-1 was synthesized according to the literature with minor modifications.[3] $Cu(NO_3)_2 \cdot 2.5H_2O$ (0.472 g, 2.03 mmol) was dissolved in 6 mL of 1:1 H_2O/DMF mixture in a 50 mL vial. Benzene-1,3,5-tricarboxylic acid (H_3BTC) (0.360 g, 1.71 mmol) was completely dissolved in slightly heated ethanol (4.5 mL) with stirring. To the Cu nitrate solution, ethanolic ligand solution, and glacial acetic acid (12 mL) were added, and placed in an oven at 55 °C. After 60 h, the mother liquor was quickly decanted, and the blue crystals were washed with dry ethanol 3 times. HKUST-1 was then activated at 130 °C for 12 h before gas sorption measurements.

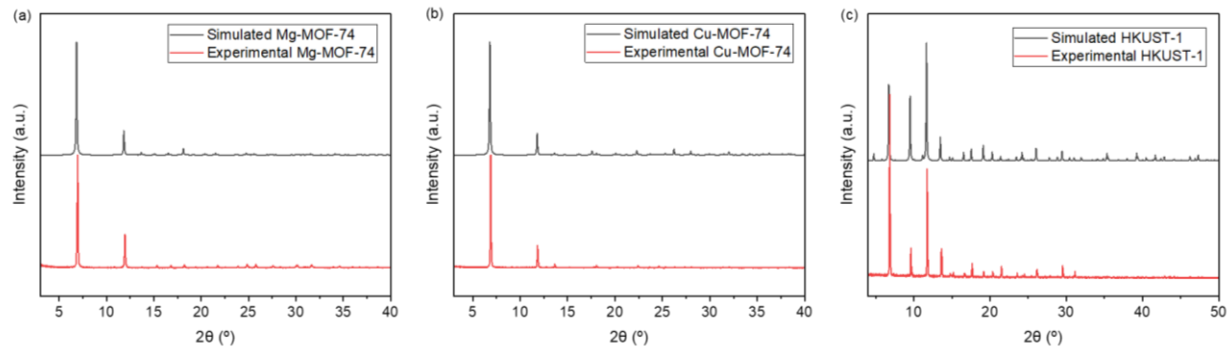

Figure S23 Simulated and experimental PXRD patterns of (a) Mg-MOF-74, (b) Cu-MOF-74, and (c) HKUST-1.

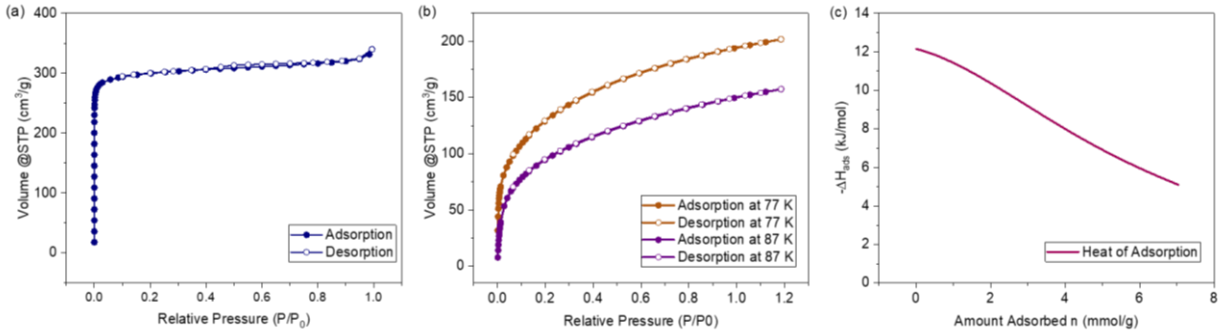

Figure S24 (a) N_2 adsorption isotherm at 77 K, (b) H_2 adsorption isotherm at 77 and 87 K up to 1.2 bar, and (c) heat of adsorption of Mg-MOF-74.

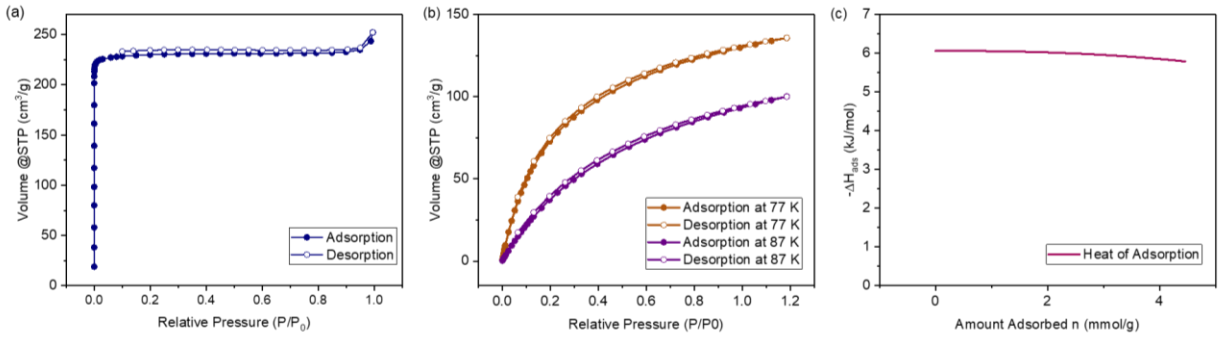

Figure S25 (a) N_2 adsorption isotherm at 77 K, (b) H_2 adsorption isotherm at 77 and 87 K up to 1.2 bar, and (c) heat of adsorption of Cu-MOF-74.

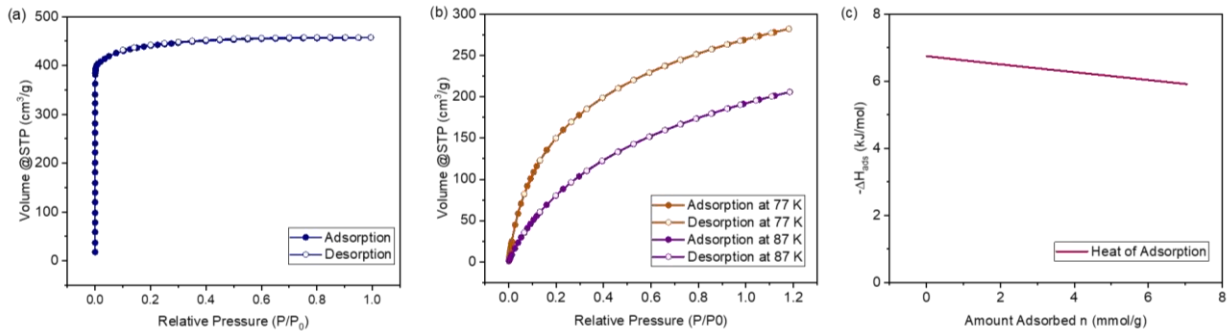

Figure S26 (a) N_2 adsorption isotherm at 77 K, (b) H_2 adsorption isotherm at 77 and 87 K up to 1.2 bar, and (c) heat of adsorption of HKUST-1.

Table S8 BET surface area, wt.% H_2 adsorbed at 77K, 1 bar and $-\Delta H_{ads}^0$ of MOF-808 and representative MOFs.

MOF	Activation temperature (°C)	BET Surface Area (m^2/g)	H_2 uptake (wt.%) at 77 K/1 bar	$-\Delta H_{ads}^0$ (kJ/mol)	Reference
MOF-808	200	2142	1.145	5.437	This study
MOF-808-ZrCu	200	1469	1.034	7.074	This study
Cu-MOF-74	150	965	1.158	6.058	2
HKUST-1	130	1729	2.398	6.749	4-5
MOF-808@Mg 2:1	200	2149	1.186	6.258	This study
Mg-MOF-74	150	1208	1.730	12.149	6

References:

1. Al-Naddaf, Q.; Rezaei, F., Multicomponent adsorptive separation of CO2, CO, CH4, N2, and H2 over core-shell zeolite-5A@MOF-74 composite adsorbents. *Chem. Eng. J.* **2019,** *384*, 123251.
2. Rosnes, M. H.; Opitz, M.; Frontzek, M.; Lohstroh, W.; Embs, J. P.; Georgiev, P. A.; Dietzel, P. D. C., Intriguing differences in hydrogen adsorption in CPO-27 materials induced by metal substitution. *J. Mater. Chem. A* **2015,** *3* (9), 4827-4839.
3. Kwon, O.; Kim, J. Y.; Park, S.; Lee, J. H.; Ha, J.; Park, H.; Moon, H. R.; Kim, J., Computer-aided discovery of connected metal-organic frameworks. *Nat. Commun.* **2019,** *10* (1), 3620.
4. Kubo, M.; Matsumoto, T.; Shimada, M. Enhancement of Hydrogen Adsorption on Spray-Synthesized HKUST-1 via Lithium Doping and Defect Creation *Mater.* [Online], 2023.
5. Rowsell, J. L. C.; Yaghi, O. M., Effects of Functionalization, Catenation, and Variation of the Metal Oxide and Organic Linking Units on the Low-Pressure Hydrogen Adsorption Properties of Metal−Organic Frameworks. *J. Am. Chem. Soc.* **2006,** *128* (4), 1304-1315.
6. Zhou, W.; Wu, H.; Yildirim, T., Enhanced H2 Adsorption in Isostructural Metal−Organic Frameworks with Open Metal Sites: Strong Dependence of the Binding Strength on Metal Ions. *J. Am. Chem. Soc.* **2008,** *130* (46), 15268-15269.